In addition to the absolute volumes of cerebral structures, we conducted two approaches of volume data analyses considering the possibility of slight brain shrinkage by long-term fixation in the PFA solution. First, absolute volumes of each cerebral structure were normalized to the whole cerebral volume (results are shown in Table 1). Then, two-way ANOVA revealed significant effects on cerebral structures ($F_{6,26} = 234524.881$, $P < 0.001$) and interactions between sexes and cerebral structures ($F_{6,26} = 4.429$, $P < 0.001$). Significantly lower volumes of cerebral cortex ($P < 0.001$) and subcortical white matter ($P < 0.05$) in females than in males were detected by post-hoc testing. As with the results of the absolute volumes, the % volumes of other cerebral structures to total cerebral volumes were not different between sexes, statistically. Second, we calculated larger % volumes in males than in females (Table 1). While the volume of amygdala in females was almost equal to that in males, 6–17% larger volumes in males rather than in females were marked in other cerebral structures (the cortex, olfactory bulb, caudate nucleus, lentiform nucleus, hippocampus and subcortical white matter).

Normalized signal ratios of short TR/TE- and T_2W-MRI intensity in subcortical and archicortical structures

The signal intensities of short TR/TE- and T_2W-MRI were normalized in the cerebral cortex, the major subcortical (i.e., the caudate nucleus and lentiform nucleus) and archicortical structures (i.e., the olfactory bulb, amygdala and hippocampus), and in the subcortical white matter. The normalized signal ratio of the short TR/TE-MRI intensity in those structures was slightly higher in males than in females (Fig. 4). Two-way ANOVA revealed significant effects on sexes ($F_{1,126} = 18.401$, $P < 0.001$) and cerebral structures ($F_{6,126} = 4.338$, $P < 0.001$), but not on their interaction. Therefore, a reduction in the signal ratio of short TR/TE-MRI intensity was found throughout the female cerebrum while post-hoc testing indicated significantly higher signal ratios only in the amygdala. In contrast, the normalized signal ratio of the T_2W-MRI intensity in each structure did not differ between sexes (Fig. 4). Two-way ANOVA revealed significant effects on cerebral structures ($F_{6,126} = 124.329$, $P < 0.001$), but not on sexes and their interaction. The significant effects on the cerebral

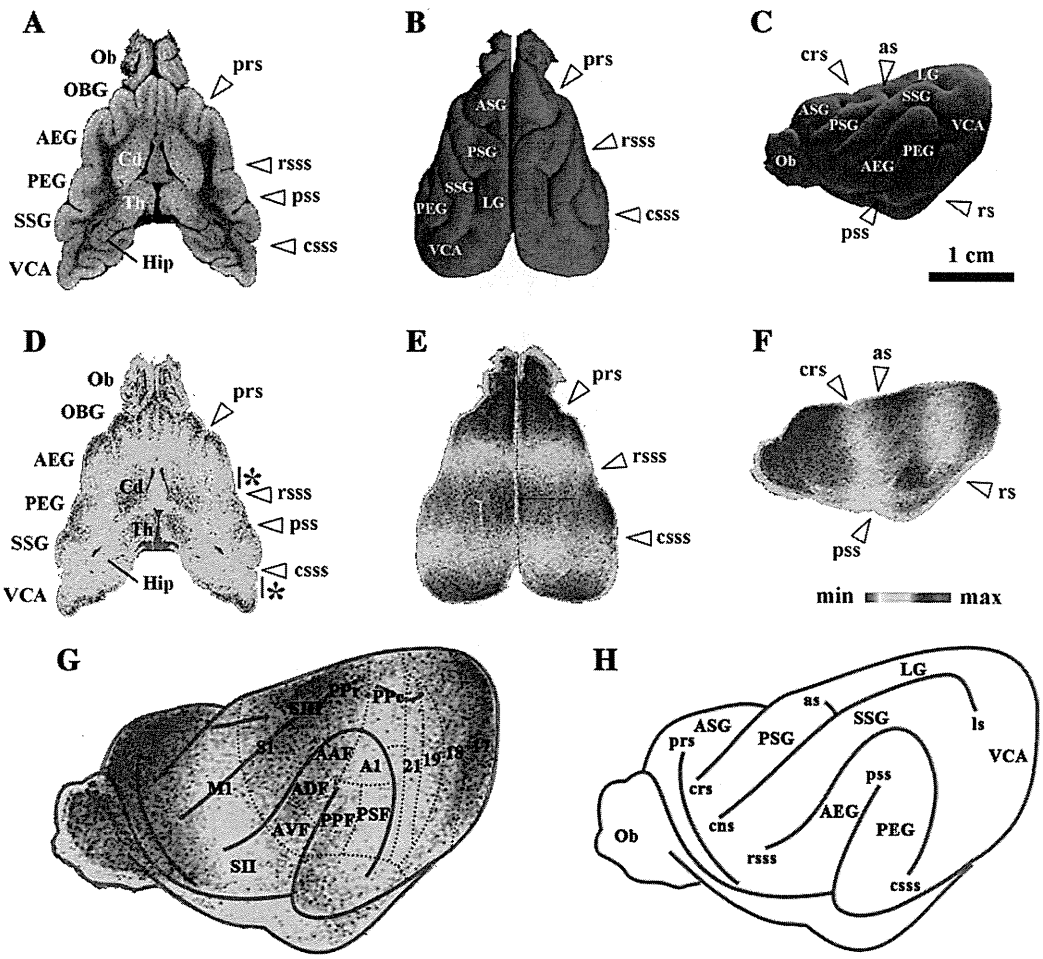

Fig. 6. Short TR/TE-MRI-based MIP color maps and axial image of short TR/TE-MRI color map representing an array of higher and lower short TR/TE-MRI transverse zones through the cerebral cortex. (A) Axial short TR/TE-MRI image of ferret cerebrum as a reference. (B) Dorsal view of three-dimensional volume-rendered images of cerebrum as a reference. (C) Lateral view (left side) of three-dimensional volume-rendered images of cerebrum as a reference. (D) Axial image of short TR/TE-MRI intensity color map of the cerebrum. Signal intensities represented on short TR/TE-MRI images of each pixel were color-coded. Red asterisks (*) in (D) indicate lower short TR/TE-MRI transverse zones of the cerebral cortex on axial short TR/TE-MRI images. (E) Dorsal view of short TR/TE-MRI-based MIP color map of the cerebrum. (F) Lateral view (left side) of short TR/TE-MRI-based MIP color map of the cerebrum. (G) Known functional cortical areas of cerebrum (modified from Manger et al., 2004; Keniston et al., 2009; Foxworthy and Meredith, 2011) overlayed on the lateral view of the MIP color map. An array of higher and lower short TR/TE-MRI transverse zones defined by MIP color map was reminiscent of the functional cortical areas. (H) Lateral view of sulcal and gyral map as a reference. A1, primary auditory cortex; AAF, anterior auditory field; ADF, anterior dorsal field; as, ancinate sulcus; AEG, anterior ectosylvian gyrus; ASG, anterior sigmoid gyrus; AVF, anterior ventral field; Cd, caudate nucleus; cns, coronal sulcus; crs, cruciate sulcus; csss, caudal suprasylvian sulcus; Hip, hippocampus; M1, primary motor cortex; Ob, olfactory bulb; OBG, orbital gyrus; PEG, posterior ectosylvian gyrus; PPc, caudal posterior parietal cortex; PPr, rostral posterior parietal cortex; prs, presylvian sulcus; PSG, posterior sigmoid gyrus; pss, pseudosylvian sulcus; rs, rhinal sulcus; rsss, rostral suprasylvian sulcus; S1, primary somatosensory cortex; SII, second somatosensory cortex; SIII, third somatosensory cortex; SSG, suprasylvian gyrus; Th, thalamus; VCA, visual cortical area.

structures revealed that signal ratios of short TR/TE- and T_2W-MRI intensity were different among each cerebral structure. Subcortical white matter, the sole white matter structure examined in the present study, was noted for having lower signal ratios of short TR/TE- and T_2W-MRI intensity than signal ratios of other cerebral structures of male and female ferrets.

Color maps of short TR/TE- and T_2W-MRI intensity and short TR/TE-MRI-based MIP

Short TR/TE- and T_2W-MRI represent the physiochemical properties of the tissues that differ among each structure of the cerebrum. Coronal images of short TR/TE- and T_2W-MRI color maps, and axial

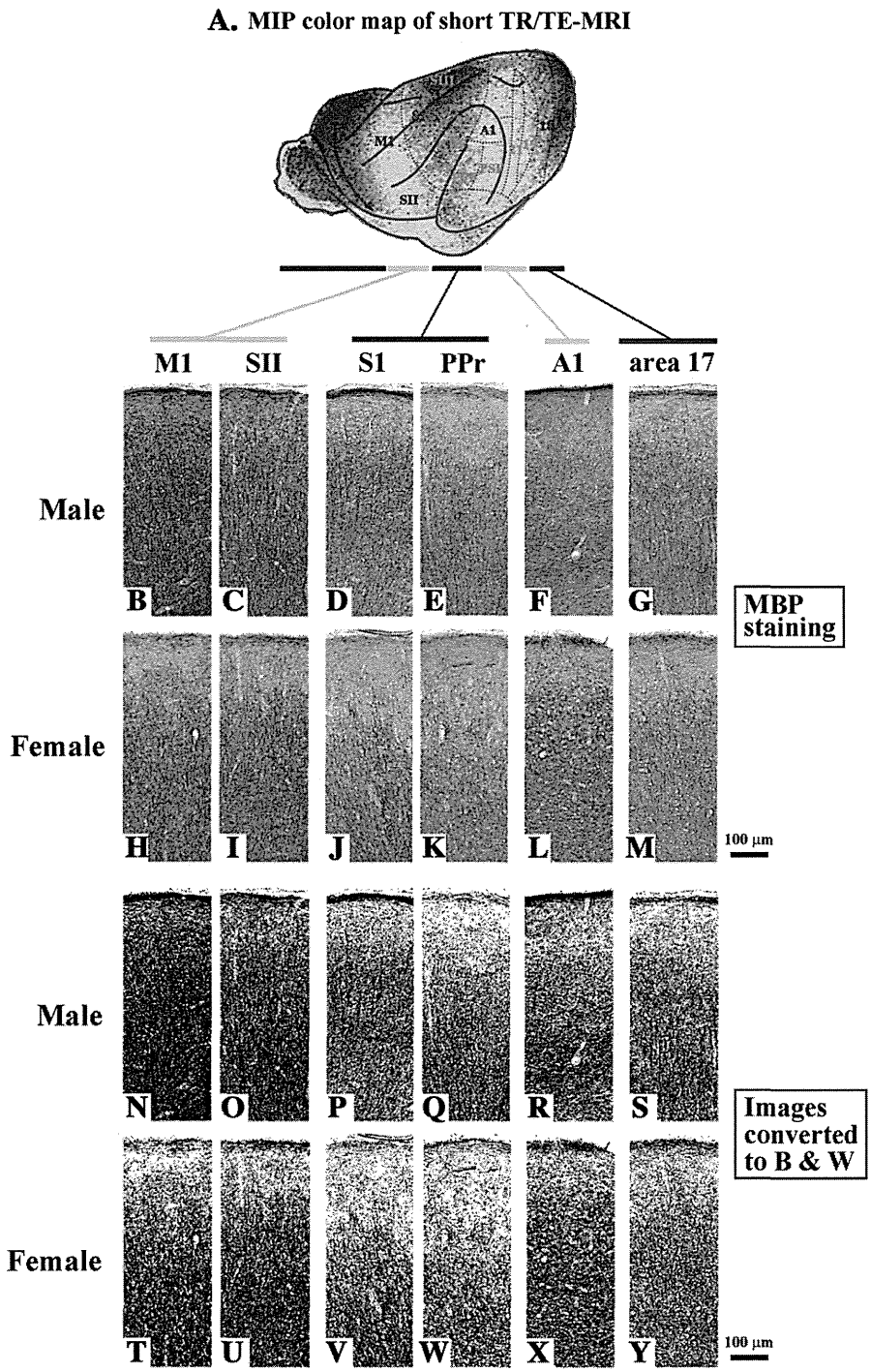

Fig. 7. Myelin basic protein (MBP) immunostaining in representative functional cortical areas of male and female ferrets. (A) Topology of each cortical area is shown by short TR/TE-MRI-based MIP color map of cerebral cortex. Photomicrographs from (B) to (M) are representative MBP-immunostained sections of rostral lower intensity zone (primary motor cortex (M1) and second somatosensory cortex (SII)), intermediate higher intensity zone (primary somatosensory cortex (S1) and rostral posterior parietal cortex (PPr)), caudal lower intensity zone (primary auditory cortex (A1)), and caudal higher intensity zone (area 17) of male (B–G) and female (H–M) ferrets. Photomicrographs in (N) to (Y) are images of MBP-immunostained sections in each cortical area converted into black and white for evaluating the density of MBP immunoreactive fibers of male (N–S) and female (T–Y) ferrets. AAF, anterior auditory field; ADF, anterior dorsal field; AVF, anterior ventral field; PPc, caudal posterior parietal cortex; SIII, third somatosensory cortex.

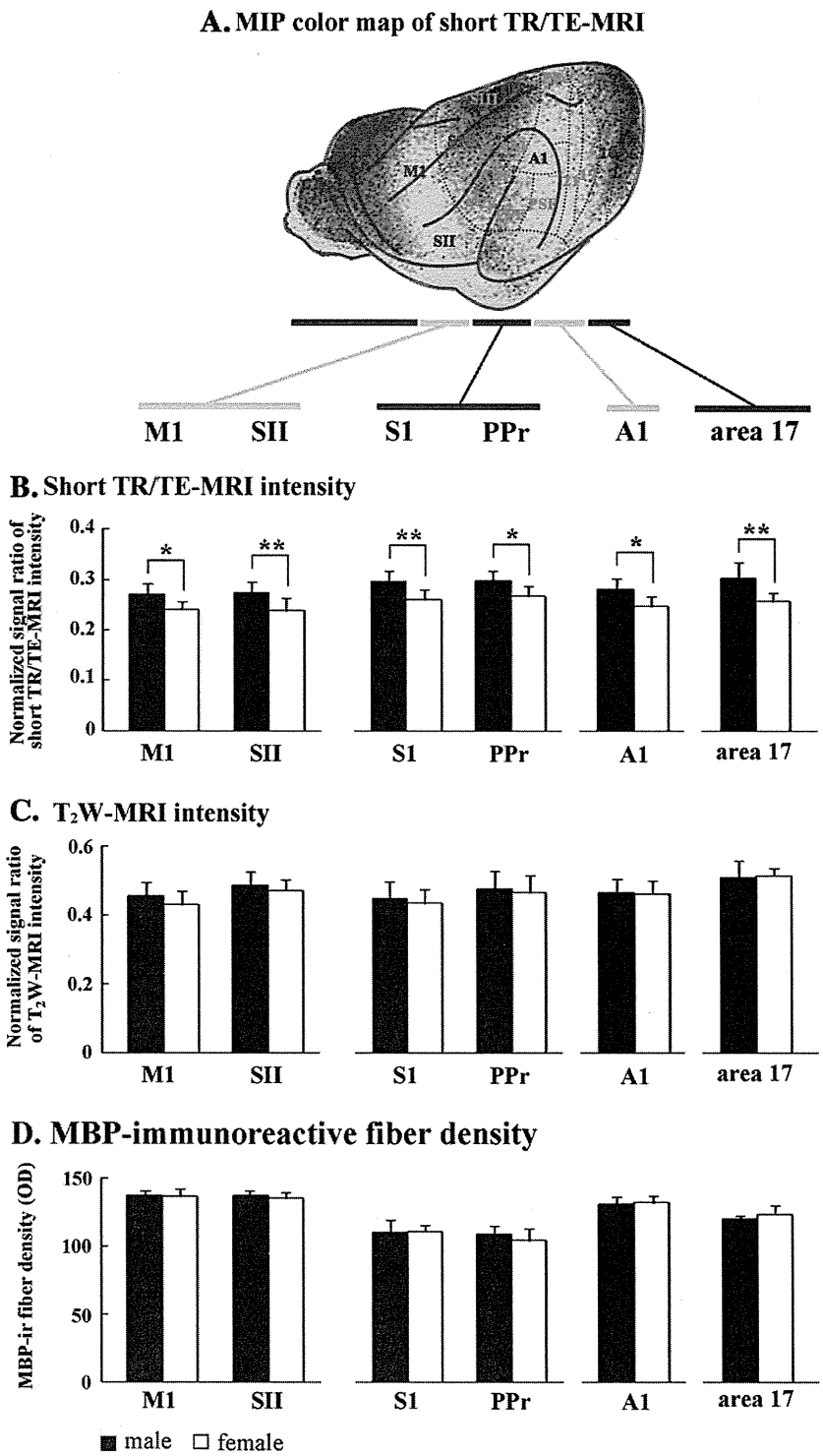

Fig. 8. Bar graphs for normalized signal ratios of short TR/TE (typical T_1-weighted parameter setting for conventional MRI) and T_2W (long TR/TE) MRI intensity, and for the density of myelin basic protein (MBP) immunoreactive (ir) fibers of representative cortical areas of male and female ferrets. Measurements of the left and right hemispheres were quantified separately, and data on each side of the hemisphere were considered to be "n = 1." (A) Topology of each cortical area is shown by short TR/TE-MRI-based MIP color map of the cerebral cortex: primary motor (M1) and second somatosensory (SII) cortices located in the rostral lower intensity zone; the primary somatosensory (S1) and rostral posterior parietal (PPr) cortices located in the intermediate higher intensity zone; primary auditory cortex (A1) located in the caudal lower intensity zone; and area 17 located in the caudal higher intensity zone. (B) Normalized signal ratios of short TR/TE-MRI intensity. For short TR/TE-MRI, two-way ANOVA revealed significant effects on sexes ($F_{1,108} = 272.010$, $P < 0.001$) and cortical areas ($F_{5,108} = 5.718$, $P < 0.001$), but not on their interaction. *: $P < 0.01$; $P < 0.001$ (*Fisher's* LSD test). (C) Normalized signal ratios of T_2W-MRI intensity. For T_2W-MRI, a significant effect was found on cortical areas ($F_{5,108} = 7.400$, $P < 0.001$), but not on sexes or interactions between cortical areas and sexes. (D) MBP-ir fiber density. With MBP immunostaining, two-way ANOVA revealed a significant effect on cortical areas ($F_{1,108} = 97.043$, $P < 0.001$), but not on sexes or interactions between cortical areas and sexes.

images of short TR/TE-MRI color maps of the male ferret cerebrum are shown in Figs. 5 and 6, respectively. Short TR/TE-MRI intensity but not T_2W-MRI intensity was organized into an alternating array of higher and lower intensity transverse zones throughout the cerebral cortex. Short TR/TE-MRI intensity in both the rostral half of the AEG and the rostral half of the VCA was relatively lower than that in other cortical regions on those axial images (* in axial image of short TR/TE-MRI color map in Fig. 6D).

Spatial distributions of the cortical regions representing higher or lower short TR/TE-MRI intensity were examined by MIP, which projected the voxels with maximum intensity in 3D. The short TR/TE-MRI-based MIP color maps revealed an alternating array of higher and lower intensity transverse zones throughout the cerebral cortex in males (Fig. 6). A similar transverse array was obtained in the female cortex. In order to determine whether such an array is the effect of inhomogeneity in the RF coil's B_1 field, we examined the MIP color map of the background signal of the medium (PFA solution) that filled the brains. No stripes of higher or lower intensity were obtained through the medium on the MIP map (see Supplement 4), suggesting that B_1 field inhomogeneity is not responsible for the observed patterns. The lower intensity transverse zones were present through the rostral one-third regions of the PSG, suprasylvian gyrus (SSG) and AEG, and through the caudal half of the PEG and the caudal half of the VCA. The known cortical areas of the ferret cerebrum (modified from Foxworthy and Meredith, 2011; Keniston et al., 2009; Manger et al., 2004) were overlayed on the present MIP color maps in Fig. 6G. The rostral lower intensity transverse zone corresponded to the M1 and SII, and the caudal lower intensity transverse zone corresponded to the A1 (Fig. 6G).

Myelin fiber density and normalized signal ratios of short TR/TE- and T_2W-MRI intensity in cortical areas

Since the signal intensity of T_1-weighted MRI through the shortening of T_1 (longitudinal relaxation time) and T_2 (transverse relaxation time) is known to be altered by myelination (Holland et al., 1986), MBP immunostaining was carried out to evaluate the degree of myelination in each cortical area. A number of MBP-immunoreactive fibers were present in the cerebral cortex, while their densities varied among the cortical areas (Fig. 7). In order to quantify the density of those fibers, captured images were converted to black and white images (Fig. 7), and the OD was measured. Two-way ANOVA revealed a significant effect on cortical areas ($F_{1,108} = 97.043$, $P < 0.001$), but not on sexes in the density of MBP immunoreactive fibers. The density of MBP-immunoreactive fibers was relatively high in the M1, SII and A1, but relatively low in the S1, PPr, and area 17 (Fig. 8).

Normalized signal ratios of the short TR/TE-MRI intensity on each cortical area were shown in Fig. 8. Two-way ANOVA revealed significant effects on sexes ($F_{1,108} = 272.010$, $P < 0.001$) and cortical areas ($F_{5,108} = 5.718$, $P < 0.001$). Post-hoc testing indicated significantly lower signal ratios in females than in males throughout cortical areas examined, i.e., the M1 ($P < 0.01$), S1 ($P < 0.001$), SII ($P < 0.001$), A1 ($P < 0.01$), PPr ($P < 0.01$), and area 17 ($P < 0.001$) (Fig. 8). Such sexual differences were not region-specific, because there was no interaction

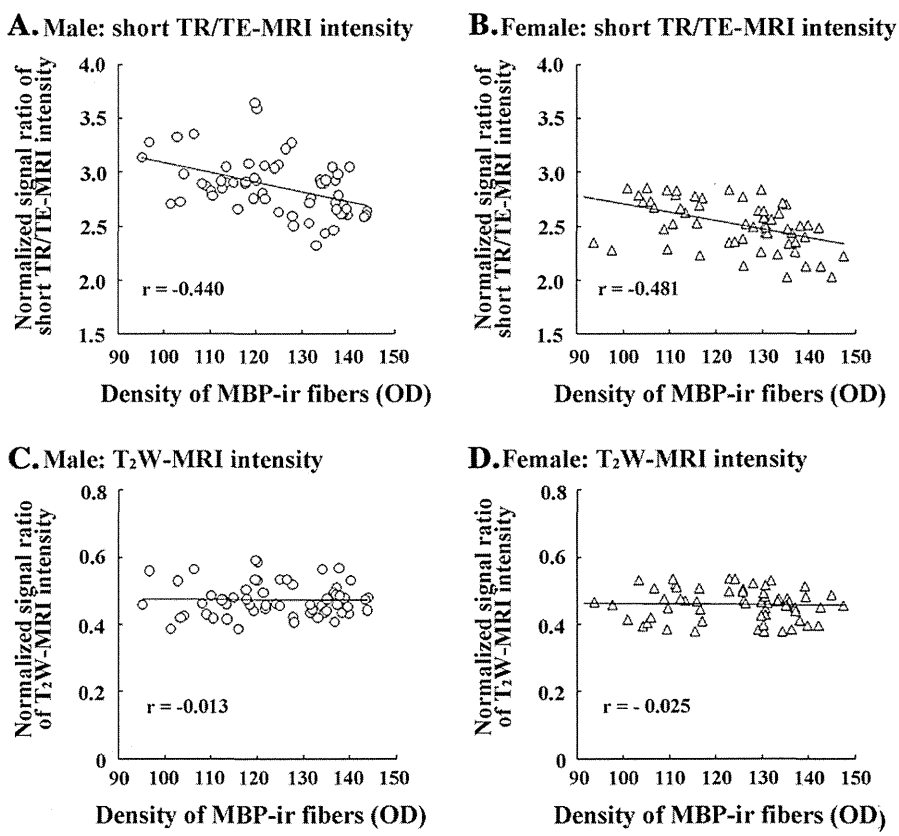

Fig. 9. Correlations of the density of myelin basic protein (MBP) immunoreactive (ir) fibers with normalized signal ratios of short TR/TE (typical T_1-weighted parameter setting for conventional MRI) and T_2W (long TR/TE) MRI in the cerebral cortex of ferrets. Measurements of left and right hemispheres were quantified separately in males (n = 5) and females (n = 5), and data on each side of the hemisphere were considered to be "n = 1." Since the ROIs were specified at 6 known cortical areas (i.e., the primary motor cortex (M1), primary somatosensory cortex (S1), secondary somatosensory cortex (SII), primary auditory cortex (A1), rostral posterior parietal cortex (PPr) and area 17), data obtained from total 60 points were plotted as circles or triangles in each graph (Y-axis: normalized signal ratio of short TR/TE- or T_2W-MRI intensity in each cortical area. X-axis: OD of MBP-ir fibers in identical cortical areas). Short TR/TE-MRI had a close negative correlation with the density of MBP immunoreactive fibers (males, r = −0.440; females, r = −0.481), but T_2W-MRI (males, r = 0.013; females, r = −0.025) did not.

between sexes and cortical areas by two-way ANOVA. It should be noted that signal ratios of short TR/TE-MRI intensity were different among cortical areas in both sexes. Relatively higher intensities, marked in the S1, PPr, and cortical area 17, were also present in the intermediate or caudal higher intensity transverse zones (Fig. 8). On the contrary, relatively lower signal ratios were marked in the M1, SII, and A1, which were present in the rostral or caudal higher intensity transverse zone in the cerebrum (Fig. 8).

The normalized signal ratio of T_2W-MRI intensity on each cortical area was shown in Fig. 8. Two-way ANOVA revealed a significant effect on cortical areas ($F_{5,108} = 7.400, P < 0.001$), but not on sexes or interactions between cortical areas and sexes (Fig. 8). Interestingly, the short TR/TE-MRI signal ratio had a close negative correlation with the density of MBP immunoreactive fibers (males, $r = -0.440$; females, $r = -0.481$), but the T_2W-MRI signal ratio did not (males, $r = 0.013$; females, $r = -0.025$) (Fig. 9). Thus, the signal intensity of short TR/TE-MRI in the cerebral cortex reflected the myelin density, and the MIP color maps of short TR/TE-MRI could reproduce the myeloarchitecture of the cerebral cortex in 3D.

Discussion

Ex vivo MRI using the fixed brain provides detailed morphology of the brain greater than that of *in vivo* MRI (Benveniste and Blackband, 2006). Several previous studies have characterized the cerebral morphology of adult ferret at various postnatal stages using MRI such as T_2-weighted MRI and DTI *in vivo* (Barnette et al., 2009; Kroenke et al., 2009; Neal et al., 2006). The present study further characterized the detailed morphology of the ferret cerebrum and its sexual dimorphism using MRI-based morphometry. Ferrets have advantages as an experimental model for studying the plasticity and development of the central nervous system. In particular, the ferret's cerebral cortical morphology matures in a regular sequence of sulcation and gyration during the first 2 postnatal weeks (Sawada and Watanabe, 2012), with a trajectory similar to that of the gyrification processes of the cerebrum of humans and non-human primates (Sawada et al., 2012). Also, the massive expansion of oSVZ with Pax6-expressing basal radial glia, which is thought to be correlated with the evolution and gyrification of the cerebral cortex (Hevner and Haydar, 2012), was confirmed during early postnatal ages (Fietz et al., 2010; Martínez-Cerdeño et al., 2012). Because experimental magnifications such as drug administration and stress loading are applied directly to the pups, the ferret is an advantageous model for studying human developmental and psychological disorders with gyrification abnormalities, i.e., schizophrenia and autism (Bonnici et al., 2007; Harden et al., 2004; Harris et al., 2004a,b; Jou et al., 2005; Kippenhan et al., 2005; Kulynych et al., 1997; Levitt et al., 2003; Nierenberg et al., 2005; Rapoport et al., 2005; Sallet et al., 2003; Vogeley et al., 2001). The present study provides MRI reference for the cerebral morphology of male and female ferrets.

In our previous study (Sawada and Watanabe, 2012), the enhanced leftward asymmetry of the cortical convolution in the visual cortex of males was observed as a sex-related morphological change in the ferret cerebrum. In the present study, sexual dimorphism of the ferret cerebrum was characterized by region-specific reductions in the volumes of the cortex and subcortical white matter found in females than in males, and by region-nonspecific changes in physiochemical properties of the cortex reflected by short TR/TE-MRI. Several studies have conducted quantitative analyses of the sexual dimorphism of cerebral morphology, such as the greater rightward bias in men than in women in the cortical volumes across all cerebral lobes except for the parietal lobe (Carne et al., 2006); overall greater thickness of the cerebral cortex in men than in women (Sowell et al., 2007); and right-dominant cortical thickness in male but not female rats (Diamond, 1987; Diamond, 1991; Stewart and Kolb, 1988). In other cerebral regions, sexual dimorphism was detected in volumes of the hippocampus, caudate nucleus and globus pallidus in humans (Giedd et al., 1997; Suzuki et al., 2005), and in the hippocampus and olfactory bulb in mice (Koshibu et al., 2004; Spring et al., 2007). A larger volume of amygdala in males than in females was marked in mice (Koshibu et al., 2004), but not in humans (Kim et al., 2012) and rhesus monkeys (Franklin et al., 2000). Although a larger volume of human amygdala in men than women was reported (Giedd et al., 1997; Goldstein et al., 2001), such a difference is considered to depend on age rather than sex (Kim et al., 2012). Therefore, sexual dimorphism of the volumes of each cerebral region differs among mammalian species. Since sex-related volume changes in left and/or right side(s) of particular regions of the cerebral cortex, amygdala and hippocampus are involved in schizophrenia (Exner et al., 2008), amnestic mild cognitive impairment, Alzheimer's disease (Skup et al., 2011), and panic disorder (Asami et al., 2009) in humans, the volumes of various cerebral regions in male and female ferrets in the present study may provide useful information for investigating neurodevelopmental and psychological disorders exhibiting sex-related prevalence.

In the present study, detailed laminar cytoarchitecture of the olfactory bulb could be reproduced by short TR/TE-MRI. In a previous study by Boretius et al. (2009), the mitral cell layer of the olfactory had been distinguished as having a low signal intensity by optimized T_2-weighted fast spin-echo MRI at 9.4 T with high resolution ($40 \times 40 \times 300$ μm). Their study further delineated cell layers of cerebral cortex, hippocampus and cerebellum. However, our procedure in T_2W-MRI measurements (7-T; resolution = $150 \times 150 \times 2000$ μm) failed to delineate the cell layers of the olfactory bulb as well as the cerebral cortex and hippocampus. Further study will be needed to establish optimal procedures of T_2W-MRI measurements for delineation of cell layers in various brain regions in ferret *ex vivo*.

In a previous study using common marmosets, T_1-weighted MRI represented myeloarchitecture in the cerebral cortex (Bock et al., 2009). The present study reveals a negative correlation of short TR/TE-MRI with the density of MBP-immunoreactive fibers in the ferret cerebral cortex. In the present study, reduced short TR/TE-MRI intensity may be related to short tissue T_1 in myelinated fibers, which is strongly influenced by a signal reduction due to T_2 shortening in the short TR/TE of high-field MRI. The cerebral cortex has natural topographic parturition defined by chemoarchitectonic staining. For example, immunostaining for non-phosphorylated forms of the neurofilament heavy chain (NFH; recognized by anti-SMI-32) and myelin staining define the regional architectural parcellation of the cortex, which is relevant to the cortical areas (Boire et al., 2005; Cruz-Rizzolo et al., 2011; Mellott et al., 2010; Van De Werd et al., 2010; van der Gucht et al., 2007). Such a chemical parcellation has been well characterized in the visual and posterior parietal cortices in ferrets (Homman-Ludiye et al., 2010; Innocenti et al., 2002; Manger et al., 2004). In the present study, short TR/TE-MRI-based MIP color maps revealed an array of higher and lower short TR/TE-MRI intensity transverse zones throughout the ferret cerebral cortex, which was reminiscent of the functional cortical areas. Therefore, the functional cortical areas relevant to myelin fiber density may be reproduced in 3D by short TR/TE-MRI-based MIP color maps.

In some gyrencephalic animals including humans, cerebral sulci are used as reproducible landmarks for delineating the cortical areas on MRI (Maudgil et al., 1998; Zilles et al., 1997). However, it is difficult to define the functional cortical areas of lissencephalic animals by non-invasive *in vivo* imaging techniques such as MRI and CT. Therefore, short TR/TE-MRI-based MIP color maps of the cerebral cortex may be useful for investigating the organization of the functional cortical areas and their abnormalities, particularly in lissencephalic animals such as rats and mice.

Normalized signal ratios of short TR/TE- and T_2W-MRI differ among tissues, and are useful for the diagnosis of injuries, diseases and developmental disorders of the brain. In the present study, an overall decrease was found in the signal ratios of short TR/TE-MRI of

the cerebral cortex and the major subcortical and archicortical structures. It is known that both shortening of T_1 and T_2 are altered by various physiochemical properties in tissues such as water diffusion (Holland et al., 1986) and magnetization transfer (Ogg and Steen, 1988). Myelination is known as one of the factors that alters the signal ratios of T_1-weighted and T_2-weighted MRIs in brain tissue (Holland et al., 1986). However, semi-quantitative immunohistochemical evaluation in the present study revealed no sex differences in myelin fiber density throughout the cerebral cortex, while the density was varied among functional cortical areas. It remains unclear why the signal ratio of short TR/TE-MRI was higher in males than in females in the present study. Other factors altering short TR/TE- and T_2W-MRI signals such as water contents of extracellular matrix and cell density (Prayer et al., 2006) may differ between sexes in the ferret cerebral tissues.

In conclusion, the present study is, to our knowledge, the first to characterize the detailed cerebral morphology of young adult ferrets and to describe its sexual dimorphism by two approaches using high-field MRI and MRI-based morphometry. As a further consideration, sexual dimorphism of the shapes and positions of each cerebral structure should be characterized in ferrets. However, since our brain samples were removed from skulls before MRI measurements, some artifact changes such as slight shrinkage of the brain tissues and reduced volume of ventricle (Ma et al., 2008) may hinder obtaining exact data regarding the shape and positions of cerebral structures. *In vivo* studies will also be needed. On the other hand, the present study provides full 3D brain coverage of MRI references for normal cerebral morphology of ferrets to investigate pathogenesis of sex-related neurodevelopmental and psychological disorders, i.e., autism (Levitt et al., 2003; Harden et al., 2004), schizophrenia (Exner et al., 2008), amnestic mild cognitive impairment, Alzheimer's disease (Skup et al., 2011), and panic disorder (Asami et al., 2009). Furthermore, short TR/TE-MRI-based MIP could visualize functional cortical areas related to myeloarchitecture in 3D. Such an approach makes it possible to investigate the functional organization of the cerebral cortex and its abnormalities, using MRI in a conventional manner.

Supplementary data to this article can be found online at http://dx.doi.org/10.1016/j.neuroimage.2013.06.024.

Acknowledgments

This study was supported by JSPS KAKENHI (23590223), and partly supported by "Funding Program for World-Leading Innovative R&D on Science and Technology (FIRST Program)" for MRI devices. The authors wish to thank Mr. Nobuhiro Nitta (Molecular Imaging Center, National Institute of Radiological Sciences, Chiba, Japan) for MRI measurements, and Ms. Misaki Watanabe (The Department of Nursing, Faculty of Medical and Health Sciences, Tsukuba International University, Tsuchiura, Ibaraki, Japan) for her generous assistance.

Conflict of interest

There are no conflicts of interest.

References

Asami, T., Yamasue, H., Hayano, F., Nakamura, M., Uehara, K., Otsuka, T., Roppongi, T., Nihashi, N., Inoue, T., Hirayasu, Y., 2009. Sexually dimorphic gray matter volume reduction in patients with panic disorder. Psychiatry Res. 173, 128–134.

Barnette, A.R., Neil, J.J., Kroenke, C.D., Griffith, J.L., Epstein, A.A., Bayly, P.V., Knutsen, A.K., Inder, T.E., 2009. Characterization of brain development in the ferret via MRI. Pediatr. Res. 66, 80–84.

Benveniste, H., Blackband, S.J., 2006. Translational neuroscience and magnetic-resonance microscopy. Lancet Neurol. 5, 536–544.

Bock, N.A., Kocharyan, A., Liu, J.V., Silva, A.C., 2009. Visualizing the entire cortical myelination pattern in marmosets with magnetic resonance imaging. J. Neurosci. Methods 185, 15–22.

Boire, D., Desgent, S., Matteau, I., Ptito, M., 2005. Regional analysis of neurofilament protein immunoreactivity in the hamster's cortex. J. Chem. Neuroanat. 29, 193–208.

Bonnici, H.M., William, T., Moorhead, J., Stanfield, A.C., Harris, J.M., Owens, D.G., Johnstone, E.C., Lawrie, S.M., 2007. Pre-frontal lobe gyrification index in schizophrenia, mental retardation and comorbid groups: an automated study. Neuroimage 35, 648–654.

Boretius, S., Kasper, L., Tammer, R., Michaelis, T., Frahm, J., 2009. MRI of cellular layer in mouse brain *in vitro*. Neuroimage 47, 1252–1260.

Carne, R.P., Vogrin, S., Litewka, L., Cook, M.J., 2006. Cerebral cortex: an MRI-based study of volume and variance with age and sex. J. Clin. Neurosci. 13, 60–72.

Clancy, B., Darlington, R.B., Finlay, B.L., 2001. Translating time across mammalian species. Neuroscience 105, 7–17.

Cruz-Rizzolo, R.J., De Lima, M.A., Ervolino, E., de Oliveira, J.A., Casatti, C.A., 2011. Cyto-, myelo- and chemoarchitecture of the prefrontal cortex of the *Cebus* monkey. BMC Neurosci. 12, 6. http://dx.doi.org/10.1186/1471-2202-12-6.

Diamond, M.C., 1987. Sex differences in the rat forebrain. Brain Res. 434, 235–240.

Diamond, M.C., 1991. Hormonal effects on the development or cerebral lateralization. Psychoneuroendocrinology 16, 121–129.

Exner, C., Nehrkorn, B., Martin, V., Huber, M., Shiratori, K., Rief, W., 2008. Sex-dependent hippocampal volume reductions in schizophrenia relate to episodic memory deficits. J. Neuropsychiatry Clin. Neurosci. 20, 227–230.

Fietz, S.A., Kelava, I., Vogt, J., Wilsch-Bräuninger, M., Stenzel, D., Fish, J.L., Corbeil, D., Riehn, A., Distler, W., Nitsch, R., Huttner, W.B., 2010. OSVZ progenitors of human and ferret neocortex are epithelial-like and expand by integrin signaling. Nat. Neurosci. 13, 690–699.

Foxworthy, W.A., Meredith, M.A., 2011. An examination of somatosensory area SIII in ferret cortex. Somatosens. Mot. Res. 28, 1–10.

Giedd, J.N., Castellanos, F.X., Rajapakse, J.C., Vaituzis, A.C., Rapoport, J.L., 1997. Sexual dimorphism of the developing human brain. Prog. Neuropsychopharmacol. Biol. Psychiatry 21, 1185–1201.

Goldstein, J.M., Seidman, L.J., Makris, N., Ahern, T., O'Brien, L.M., Caviness Jr., V.S., Kennedy, D.N., Faraone, S.V., Tsuang, M.T., 2001. Normal sexual dimorphism of the adult human brain assessed by *in vivo* magnetic resonance imaging. Cereb. Cortex 11, 490–497.

Harden, A.Y., Jou, R.J., Keshavan, M.S., Varma, R., Minshew, N.J., 2004. Increased frontal cortical folding in autism: a preliminary MRI study. Psychiatry Res. 131, 263–268.

Harris, J.M., Yates, S., Miller, P., Best, J.J.K., Johnstone, E.C., Lawrie, S.M., 2004a. Gyrification in first-episode schizophrenia: a morphometric study. Biol. Psychiatry 55, 141–147.

Harris, J.M., Whalley, H., Yates, S., Miller, P., Johnstone, E.C., Lawrie, S.M., 2004b. Abnormal cortical folding in high-risk individuals: a predictor for the development of schizophrenia? Biol Psychiatry 56, 182–189.

Hevner, R.F., Haydar, T.F., 2012. The (not necessarily) convoluted role of basal radial glia in cortical neurogenesis. Cereb. Cortex 22, 465–468.

Holland, B.A., Haas, D.K., Norman, D., Brant-Zawadzki, M., Newton, T.H., 1986. MRI of normal brain maturation. Am. J. Neuroradiol. 7, 201–208.

Homman-Ludiye, J., Manger, P.R., Bourne, J.A., 2010. Immunohistochemical parcellation of the ferret (*Mustela putorius*) visual cortex reveals substantial homology with the cat (*Felis catus*). J. Comp. Neurol. 518, 4439–4462.

Innocenti, G.M., Manger, P.R., Masiello, I., Colon, I., Tetton, L., 2002. Architecture and callosal connections of visual areas 17, 18, 19 and 21 in the ferret (*Mustela putoris*). Cereb. Cortex 12, 411–422.

Jou, R.J., Hardan, A.Y., Keshavan, M.S., 2005. Reduced cortical folding in individuals at high risk for schizophrenia: a pilot study. Schizophr. Res. 75, 309–313.

Keniston, L.P., Allman, B.L., Meredith, M.A., Clemo, H.R., 2009. Somatosensory and multisensory properties of the medial bank of the ferret rostral suprasylvian sulcus. Exp. Brain Res. 196, 239–251.

Kim, H.J., Kim, N., Kim, S., Hong, S., Park, K., Lim, S., Park, J.M., Na, B., Chae, Y., Lee, J., Yeo, S., Choe, I.H., Cho, S.Y., Cho, G., 2012. Sex differences in amygdala subregions: evidence from subregional shape analysis. Neuroimage 60, 2054–2661.

Kippenhan, J.S., Olsen, R.K., Mervis, C.B., Morris, C.A., Kohn, P., Meyer-Lindenberg, A., Berman, K.F., 2005. Genetic contributions to human gyrification: sulcal morphometry in Williams syndrome. J. Neurosci. 25, 7840–7846.

Koshibu, K., Levitt, P., Ahrens, E.T., 2004. Sex-specific, postpuberty changes in mouse brain structures revealed by three-dimensional magnetic resonance microscopy. Neuroimage 22, 1636–1645.

Koyanagi, Y., Sawada, K., Sakata-Haga, H., Jeong, Y.G., Fukui, Y., 2006. Increased serotonergic innervation of lumbosacral motoneurons of rolling mouse Nagoya in correlation with abnormal hindlimb extension. Anat. Histol. Embryol. 35, 387–392.

Kroenke, C.D., Taber, E.N., Leigland, L.A., Knutsen, A.K., Bayly, P.V., 2009. Regional patterns of cerebral cortical differentiation determined by diffusion tensor MRI. Cereb. Cortex 19, 2916–2929.

Kulynych, J.J., Luevano, L.F., Jones, D.W., Weinberger, D.R., 1997. Cortical abnormality in schizophrenia: an *in vivo* application of the gyrification index. Biol. Psychiatry 41, 995–999.

Lawes, I.N.C., Andrews, P.L.R., 1998. Neuroanatomy of the ferret brain, In: Fox (Ed.), Biology and Diseases of the Ferret, 2nd ed. Lippincott Williams and Wilkins, pp. 71–102.

Levitt, J.G., Blanton, R.E., Smalley, S., Thompson, P.M., Guthrie, D., McCracken, J.T., Sadoun, T., Heinichen, L., Toga, A.W., 2003. Cortical sulcal maps in autism. Cereb. Cortex 13, 728–735.

Ma, Y., Smith, D., Hof, P.R., Foerster, B., Hamilton, S., Blackband, S.J., Yu, M., Benveniste, H., 2008. *In vivo* 3D digital atlas database of the adult C57BL/6J mouse brain by magnetic resonance microscopy. Front. Neuroanat. 2, 1. http://dx.doi.org/10.3389/neuro.05.001.2008.

Maher, J.A., DeStefano, J., 2004. The ferret: an animal model to study influenza virus. Lab. Anim. 33, 50–53.

Manger, P.R., Nakamura, H., Valentiniene, S., Innocenti, G.M., 2004. Visual areas in the lateral temporal cortex of the ferret (*Mustela putorius*). Cereb. Cortex 14, 676–689.

Martínez-Cerdeño, V., Cunningham, C.L., Camacho, J., Antczak, J.L., Prakash, A.N., Cziep, M.E., Walker, A.I., Noctor, S.C., 2012. Comparative analysis of the subventricular zone in rat, ferret and macaque: evidence for an outer subventricular zone in rodents. PLoS One 7, e30178.

Maudgil, D.D., Free, S.L., Sisodiya, S.M., Lemieux, L., Woermann, F.G., Fish, D.R., Shorvon, S.D., 1998. Identifying homologous anatomical landmarks on reconstructed magnetic resonance images of the human cerebral cortical surface. J. Anat. 193, 559–571.

Mellott, J.G., Van der Gucht, E., Lee, C.C., Carrasco, A., Winer, J.A., Lomber, S.G., 2010. Areas of cat auditory cortex as defined by neurofilament proteins expressing SMI-32. Hear. Res. 267, 119–136.

Neal, J., Takahashi, M., Silva, M., Tiao, G., Walsh, C.A., Sheen, V.L., 2006. Insights into the gyrification of developing ferret brain by magnetic resonance imaging. J. Anat. 210, 66–77.

Nierenberg, J., Salisbury, D.F., Levitt, J.J., David, E.A., McCarley, R.W., Shenton, M.E., 2005. Reduced left angular gyrus volume in first-episode schizophrenia. Am. J. Psychiatry 162, 1539–1541.

Ogg, R.J., Steen, R.G., 1988. Age-related changes in brain T_1 are correlated with iron concentration. Magn. Reson. Med. 40, 749–753.

Poluch, S., Jablonska, B., Juliano, S.I., 2008. Alteration of interneuron migrationin a ferret model of cortical dysplasia. Cereb. Cortex 18, 78–92.

Prayer, D., Kasprian, G., Krampl, E., Ulm, B., Witzani, L., Prayer, L., Brugger, P.C., 2006. MRI of normal fetal brain development. Eur. J. Radiol. 57, 199–216.

Rapoport, J.L., Addington, A., Frangou, S., 2005. The neurodevelopmental model of schizophrenia: what can very early onset cases tell us? Curr. Psychiatry Rep. 7, 81–82.

Sallet, P.C., Elkis, H., Alves, T.M., Oliveira, J.R., Sassi, E., Campi de Castro, C., Busatto, G.F., Gattaz, W.F., 2003. Reduced cortical folding in schizophrenia: an MRI morphometric study. Am. J. Psychiatry 160, 1606–1613.

Sawada, K., Watanabe, M., 2012. Development of cerebral sulci and gyri in ferrets (*Mustela putorius*). Congenit. Anom. (Kyoto) 52, 168–175.

Sawada, K., Fukunishi, K., Kashima, M., Saito, S., Sakata-Haga, H., Aoki, I., Fukui, Y., 2012. Fetal gyrification in cynomolgus monkeys: a concept of developmental stages of gyrification. Anat. Rec. (Hoboken) 295, 1065–1074.

Schlaepfer, T.E., Harris, G.J., Tien, A.Y., Peng, L., Lee, S., Pearlson, G.D., 1995. Structural differences in the cerebral cortex of healthy female and male subjects: a magnetic resonance imaging study. Psychiatry Res. 11, 129–135.

Sheehan, D.C., Hrapchak, B.B., 1980. Theory and Practice of Histotechnology, 2nd ed. Battelle Press, Columbus/Richland.

Skup, M., Zhu, H., Wang, Y., Giovanello, K.S., Lin, J.A., Shen, D., Shi, F., Gao, W., Lin, W., Fan, Y., Zhang, H., 2011. Sex differences in grey matter atrophy patterns among AD and aMCI patients: results from ADNI. Neuroimage 56, 890–906.

Smart, I.H., McSherry, G.M., 1986. Gyrus formation in the cerebral cortex in the ferret. I. Description of the external histological changes. J. Anat. 146, 141–152.

Sowell, E.R., Peterson, B.S., Kan, E., Woods, R.P., Yoshii, J., Bansal, R., Xu, D., Zhu, H., Thompson, P.M., Toga, A.W., 2007. Sex differences in cortical thickness mapped in 176 healthy individuals between 7 and 87 years of age. Cereb Cortex 17, 1550–1560.

Spring, S., Lerch, J.P., Henkelman, R.M., 2007. Sexual dimorphism revealed in the structure of the mouse brain using three-dimensional magnetic resonance imaging. Neuroimage 35, 1424–1433.

Stewart, J., Kolb, B., 1988. The effects of neonatal gonadectomy and prenatal stress on cortical thickness and asymmetry in rats. Behav. Neural Biol. 49, 344–360.

Suzuki, M., Hagino, H., Nohara, S., Zhou, S.Y., Kawasaki, Y., Takahashi, T., Matsui, M., Seto, H., Ono, T., Kurachi, M., 2005. Male-specific volume expansion of the human hippocampus during adolescence. Cereb. Cortex 15, 187–193.

Tao, J.D., Barnette, A.R., Griffith, J.L., Neil, J.J., Inder, T.E., 2012. Histopathologic correlation with diffusion tensor imaging after chronic hypoxia in the immature ferret. Pediatr. Res. 71, 192–198.

Van de Werd, H.J., Rajkowska, G., Evers, P., Uylings, H.B., 2010. Cytoarchitectonic and chemoarchitectonic characterization of the prefrontal cortical areas in the mouse. Brain Struct. Funct. 214, 339–353.

Van der Gucht, E., Hof, P.R., Van Brussel, L., Burnat, K., Arckens, L., 2007. Neurofilament protein and neuronal activity markers define regional architectonic parcellation in the mouse visual cortex. Cereb. Cortex 17, 2805–2819.

Vogeley, K., Tepest, R., Pfeiffer, U., Schneider-Axmann, T., Maier, W., Honer, W.G., Falkai, P., 2001. Right frontal hypergyria differentiation in affected and unaffected siblings from families multiply affected with schizophrenia: a morphometric MRI study. Am. J. Psychiatry 158, 494–496.

Wright, I.C., McGuire, P.K., Poline, J.B., Travere, J.M., Murray, R.M., Frith, C.D., Frackowiak, R.S., Friston, K.J., 1995. A voxel-based method for the statistical analysis of gray and white matter density applied to schizophrenia. Neuroimage 2, 244–252.

Zilles, K., Schleicher, A., Langemann, C., Amunts, K., Morosan, P., Palomero-Gallagher, N., Schormann, T., Mohlberg, H., Bürgel, U., Steinmetz, H., Schlaug, G., Roland, P.E., 1997. Quantitative analysis of sulci in the human cerebral cortex: development, regional heterogeneity, gender difference, asymmetry, intersubject variability and cortical architecture. Hum. Brain Mapp. 5, 218–221.

Published OnlineFirst May 21, 2013; DOI: 10.1158/0008-5472.CAN-12-3837

Cancer Research

Manganese-Enhanced MRI Reveals Early-Phase Radiation-Induced Cell Alterations *In Vivo*

Shigeyoshi Saito, Sumitaka Hasegawa, Aiko Sekita, et al.

Cancer Res 2013;73:3216-3224. Published OnlineFirst May 21, 2013.

Published OnlineFirst May 21, 2013; DOI: 10.1158/0008-5472.CAN-12-3837

Integrated Systems and Technologies

Cancer Research

Manganese-Enhanced MRI Reveals Early-Phase Radiation-Induced Cell Alterations *In Vivo*

Shigeyoshi Saito[1,2], Sumitaka Hasegawa[2], Aiko Sekita[2], Rumiana Bakalova[2], Takako Furukawa[2], Kenya Murase[1], Tsuneo Saga[2], and Ichio Aoki[2]

Abstract

For tumor radiotherapy, the *in vivo* detection of early cellular responses is important for predicting therapeutic efficacy. Mn^{2+} is used as a positive contrast agent in manganese-enhanced MRI (MEMRI) and is expected to behave as a mimic of Ca^{2+} in many biologic systems. We conducted *in vitro* and *in vivo* MRI experiments with Mn^{2+} to investigate whether MEMRI can be used to detect cell alterations as an early-phase tumor response after radiotherapy. Colon-26 cells or a subcutaneously grafted colon-26 tumor model were irradiated with 20 Gy of X-rays. One day after irradiation, a significant augmentation of G_2–M-phase cells, indicating a cell-cycle arrest, was observed in the irradiated cells in comparison with the control cells, although both early and late apoptotic alterations were rarely observed. The MEMRI signal in radiation-exposed tumor cells (R_1: 0.77 ± 0.01 s^{-1}) was significantly lower than that in control cells (R_1: 0.82 ± 0.01 s^{-1}) *in vitro*. MEMRI signal reduction was also observed in the *in vivo* tumor model 24 hours after irradiation (R_1 of radiation: 0.97 ± 0.02 s^{-1}, control: 1.10 ± 0.02 s^{-1}), along with cell-cycle and proliferation alterations identified with immunostaining (cyclin D1 and Ki-67). Therefore, MEMRI after tumor radiotherapy was successfully used to detect cell alterations as an early-phase cellular response *in vitro* and *in vivo*. *Cancer Res; 73(11); 3216–24. ©2013 AACR.*

Introduction

Radiotherapy involves the use of high-energy X-rays or charged particles to treat malignancies with the intention of destroying or inactivating cancer cells while preserving normal tissue integrity (1–4). Many types of biomarkers are used to detect cell viability and responses after radiotherapy *in vitro*. Although cell apoptosis is an important marker, apoptosis after radiation is observed only in limited cell types, such as hematopoietic and germ cells. In addition, radiation exposure immediately induces a significant G_2 cell-cycle arrest in many types of tumor cells (5), as well as prolonged G_1 cell-cycle arrest in normal fibroblast and ependymal cells (6, 7). The appearance ratio of the cell-cycle arrest linearly correlates with the radiation dose and cell viability in both normal and tumor cells (8). In addition, radiation-induced cell-cycle arrest can be linked to irreversible growth arrest, such as senescence-like growth arrest (SLGA), which is associated with the expression of senescence-associated β-galactosidase (SA-β-gal; ref. 9). Thus, cell-cycle arrest and alteration can be an early biomarker for evaluating therapeutic efficiency immediately after radiotherapy.

The divalent manganese ion (Mn^{2+}) has long been known as a positive intracellular MRI contrast agent because of its ability to alter the longitudinal relaxation of water protons. Manganese-enhanced MRI (MEMRI) provides a unique opportunity to study neuronal activation and architecture (10–12). The underlying principle of MEMRI lies in the fact that Mn^{2+} behaves in a manner similar to the calcium ion (Ca^{2+}) in many biologic systems (13). Extracellular Mn^{2+} can enter cells through *N*-methyl-D-aspartate (NMDA) receptors for glutamate (14) and/or voltage-gated calcium channels (15). Previous studies have found that MEMRI is useful for the *in vivo* visualization of tumors such as those arising from head and neck region (16, 17). There are several reports, discussing the factors associated with Mn enhancement and tumor uptake. The tumor cell uptake of Mn^{2+} is linked to the proliferation rate *in vitro* of human tumor cells (18). In addition, Mn^{2+} is considered to be a cell viability indicator in myocardial infarction (19, 20). Therefore, it is possible that radiation-induced cell-cycle alteration and the associated suppression of cell proliferation can be detected from the alterations in MEMRI signal enhancement.

The goal of this study was to test the hypothesis that MEMRI can be used to detect radiation-induced alterations as an early-phase tumor response after radiotherapy. In this study, we evaluated Mn^{2+} uptake in a colon cancer cell line and a

Authors' Affiliations: [1]Department of Medical Physics and Engineering, Division of Medical Technology and Science, Faculty of Health Science, Graduate School of Medicine, Osaka University, Osaka and [2]Molecular Imaging Center, National Institute of Radiological Sciences, Chiba, Japan

Note: Supplementary data for this article are available at Cancer Research Online (http://cancerres.aacrjournals.org/).

Corresponding Author: Ichio Aoki, Molecular Imaging Center, National Institute of Radiological Sciences, Molecular Imaging Building 3F, Anagawa 4-9-1, Inage, Chiba 263-8555, Japan. Phone: 81-43-206-3272; Fax: 81-43-206-3276; E-mail: aoki@nirs.go.jp

doi: 10.1158/0008-5472.CAN-12-3837

Published OnlineFirst May 21, 2013; DOI: 10.1158/0008-5472.CAN-12-3837

subcutaneous grafted mouse model by *in vitro/in vivo* MEMRI after X-ray exposure (20 Gy).

Materials and Methods

Colon cancer cells and *in vitro* irradiation experiment

The murine colon cancer cell line (colon-26) was maintained in Dulbecco's Modified Eagle Medium (DMEM; Sigma-Aldrich Japan) supplemented with 10% fetal calf serum (Nichirei) and 1% penicillin–streptomycin (Invitrogen Japan K.K.). Cells were cultured under high humidity with 5% CO_2 at 37°C. After incubation for 4 days, the colon-26 cells underwent a single exposure to X-rays at a dose of 20 Gy. The X-ray exposure conditions were: peak voltage of 200 kV, current of 20 mA, filter consisting of 0.5 mm Cu + 0.5 mm Al, a distance between the focus and objective of 550 mm and a dose rate of 1.2 to 1.3 Gy/min. The radiation dose and colon-26 cell type were selected as a "less apoptotic model" based on the evidence described in a previous report (21).

In vitro Mn^{2+} uptake study by MRI

We prepared 6 colon-26 cell pellets (control group, 3; radiation exposure group, 3) for MRI experiments at 24 hours after irradiation. The *in vitro* MRI acquisitions were carried out using a 7-T, 40 cm bore MRI magnet (Kobelco and Jastec) interfaced with a Bruker console (BioSpec, Bruker Biospin). A birdcage coil (38 mm inner diameter, transmission and reception; Rapid Biomedical) was used for the measurement of tumor cell samples. The samples were maintained at approximately 23°C.

Manganese chloride ($MnCl_2$; $MnCl_2$-$4H_2O$, Sigma-Aldrich Japan) was dissolved in the DMEM at a concentration of 0.1 mmol/L. The cells were incubated in the medium, either with or without $MnCl_2$, for 30 minutes at 37°C under 5% CO_2. After incubation, the medium was carefully removed by washing twice with PBS. The cells were harvested and dissociated with trypsin, transferred to PCR tubes, and cell pellets were collected by centrifugation. For the T_1-weighted image (T_1WI), a 2-dimensional (2D), single-slice image was obtained using a conventional spin echo (SE) sequence with the following parameters: repetition time (TR) = 350 ms, echo time (TE) = 9.57 ms, matrix size = 256 × 256, field of view (FOV) = 40.0 × 40.0 mm^2, slice thickness (ST) = 1.0 mm, fat suppression preparation (Fat-Sup) = on, number of acquisitions (NA) = 8, and slice orientation = sagittal. For this imaging sequence, the nominal voxel resolution was 156 × 156 × 1,000 μm^3. The total acquisition time for the T_1WI was 11 minutes and 56 seconds. For the inversion recovery, 2D, single-slice inversion recovery MRI was carried out using rapid acquisition with relaxation enhancement (RARE) acquisition for the T_1 map calculation with the following parameters: TR = 10,000 ms; TE = 10 ms; inversion time = 51, 100, 200, 400, 800, 1,600, 3,200, or 6,400 ms; matrix size = 256 × 256; slice orientation = sagittal (same slice orientation as that used for the T_1WI); FOV = 40.0 × 40.0 mm^2; ST = 1.0 mm; Fat-Sup = on; RARE factor = 4; and NA = 1. For this image, the nominal voxel resolution was 156 × 156 × 1,000 μm^3. The total acquisition time for inversion recovery MRI was 49 minutes and 27 seconds. The quantitative T_1 maps were calculated by conducting nonlinear least squares fitting using inversion-recovery MRI. Regions of interest (ROI) were defined on pelleted cell regions. The R_1 values in the ROI were calculated as the inverses of the T_1 values. All calculations and analyses were carried out using the MRVision image analysis software (Version 1.5.8, MRVision Co.).

Flow cytometry for cell viability and cell-cycle assays

Cell apoptosis and cycle alterations were measured using Guava Viacount and Guava Cell Cycle Reagents (Guava Technologies Inc.), followed by analysis of the cells using a Guava PCA machine (Guava Technologies Inc.). Cells were placed in 4 plates and adhered overnight for 24 hours after radiation exposure. Cells were stained with Guava Viacount and Cell Cycle Reagents according to the manufacturer's instructions.

In vivo animal model and radiation exposure

The Animal Welfare Committee of our Institution approved all studies. Male BALB/c nu/nu mice (n = 17, 21.3 ± 1.4 g, 8 weeks old; Japan SLC) were rested for 1 week before the experiment. The animals had free access to food and water and were kept under standard laboratory conditions in a specific pathogen-free environment, at 22°C to 23°C, with approximately 50% humidity, and a 12:12-hour light/dark cycle. Colon-26 cells (1×10^7) were injected subcutaneously into both legs of the male BALB/c nu/nu mice. Seven days after the injection, the tumor-bearing mice were subjected to MRI and histologic experiments. All mice underwent a single X-ray exposure of the left leg (the right legs were covered by a 1 cm thick lead layer) at a dose of 20 Gy on day 7 after inoculation of colon-26 cells. The X-ray exposure conditions were as follows: peak voltage of 200 kV, current of 20 mA, filter consisting of 0.5 mm Cu + 0.5 mm Al, a distance between the focus and objective of 550 mm, and a dose rate of 1.2 to 1.3 Gy/min. The male BALB/c nu/nu mice were divided into 2 groups (for MRI study, n = 10; for tumor growth study, n = 7). Following the radiation exposure, all mice, both control and radiation exposed, were maintained under 12:12 hour light/dark cycles until the MRI and tumor growth experiment.

In vivo MRI study

The mice were anesthetized with 2.0% isoflurane and placed in the prone position; the anesthesia was maintained at this level for MRI scanning. During the experiment, a warm flow of air over the animal maintained the body temperature at 37.0°C. The respiratory rate was maintained and monitored throughout the experiment using a rodent ventilator (MRI-1, CWE, Inc.). Before the T_1WI acquisitions, scout images were acquired, and quantitative T_2 mapping was carried out to localize the tumor. T_2 mapping was done for the assessment of necrosis in the tumors using a multi-slice, multi-echo SE sequence (TR = 3,000 ms, slice thickness = 1 mm, FOV = 40.0 × 40.0 mm, matrix = 256 × 256, slice orientation = transaxial, number of repetitions = 1), with echo times ranging from 10 to 140 ms in steps of 10 milliseconds. The total acquisition time was 10 minutes and 20 seconds.

T_1WI acquisition and quantitative T_1 mapping were carried out in the following order: preadministration (control), gadolinium (Gd)-enhanced, and Mn-enhanced experiments. First,

Published OnlineFirst May 21, 2013; DOI: 10.1158/0008-5472.CAN-12-3837

one set of T_1WIs and a T_1 map were acquired as baseline data before the administration of Gd. Second, the T_1WI and T_1 map acquisition set was repeated 4 times every 16 minutes after the administration of gadopentetate dimeglumine (Gd-DTPA). Gd-DTPA (150 μmol/kg; Bayer Japan) was diluted to a concentration of 50 mmol/L with saline and injected intravenously to evaluate tumor vasculature. A waiting time of 90 minutes was included after the first and second steps to avoid potential Gd retention in tumors. Before the administration of $MnCl_2$, we confirmed that the Gd-DTPA–related signal had returned to the baseline level. Third, T_1WI and T_1 map acquisition sets were repeated 4 times every 16 minutes after starting the Mn infusion. Before the administration, 100 mmol/L $MnCl_2$ ($MnCl_2$-$4H_2O$, Sigma-Aldrich Japan) was dissolved in distilled water and diluted to 50 mmol/L with saline to match the osmotic pressure of blood. We slowly infused the 50 mmol/L, osmotic pressure-controlled $MnCl_2$ solution (380 μmol/kg) at a rate of 0.4 mL/h through the tail vein using a syringe pump (KDS-100, KD scientific, Inc.). In subcutaneous tumors, a 2D, single-slice T_1WI was obtained using a conventional SE sequence with the following parameters: TR = 350 ms, TE = 9.57 ms, matrix size = 256 × 256, FOV = 40.0 × 40.0 mm^2, ST = 1.0 mm, Fat-Sup = on, and NA = 4. The slice orientation was transverse. For these images, the nominal voxel resolution was 156 × 156 × 1,000 μm^3. The total acquisition time was 5 minutes and 7 seconds. T_1 mapping was carried out with a single-slice 2D Look-Locker sequence (TR = 10,000 ms, TE = 10 ms, ST = 1.0 mm, matrix size = 128 × 64, FOV = 25.6 × 12.8 mm^2, NA = 1) and acquired over a period of 10 minutes and 40 seconds. For ROI studies, the first image set of 4 Gd-DTPA administration sets and third image set of 4 Mn administration sets were used. The ROIs of the subcutaneous tumor core and peripheral area were defined by the following methods. The outlines of the ROIs (ROI_{out}) were manually delineated on the T_1WI. Gd-enhanced areas over the threshold level (+2 SDs of the mean signal intensity of the ROI_{out} in the control image) were then defined as the peripheral areas using first image set after Gd-DTPA injection. The peripheral areas were excluded from the ROI_{out}. The areas that excluded the peripheral areas from the ROI_{out} were defined as the tumor core areas.

Histology

All tumors were studied histologically to clarify the source of the T_1 change. Mice were euthanized by pentobarbital (1.0 mL/animal; Dainippon-Sumitomo Pharmaceutical) overdose after the MRI scans and were prepared for histology by transcardiac perfusion with saline-containing heparin followed by 4% paraformaldehyde (Otsuka Pharmaceutical Co., Ltd.). Tissues were embedded in paraffin and transaxially sectioned into 4 μm thick sections, which were then placed on slides at the locations and orientations corresponding to the MRI slices. The slides were processed for cyclin D1 (Nichirei Biosciences Inc.), Ki-67 (Dako Japan Inc.), and activated caspase-3 (Cell Signaling Technology Japan) staining. After visualization with diaminobenzidine (DAB; DAKO Japan Inc.), tissue sections were briefly counterstained with hematoxylin. Three types of staining were conducted for each tumor. Cyclin D1 (for the detection of cell-cycle alterations) and Ki-67 (for the assessment of tumor proliferation) were identified as follows; (i) the brightness and contrast were automatically optimized using Photoshop (Ver. 8.0.1, Adobe, Inc.); (ii) the brown-stained positive cells were enhanced and converted to a black and white binary map using the "Make binary" plug-in of ImageJ (Ver.1.40g, NIH); (iii) the total area of the black regions of the binary map was measured using the "ROI" and "Measure" plug-ins of ImageJ; (iv) the ratio of the positive cell area to the total area was calculated. To identify cells that underwent apoptosis as a result of radiation exposure, the number of positive cells per square millimeter of tumor was calculated in the activated caspase-3–stained slices.

Tumor growth study

In 7 tumor-bearing mice, 2 perpendicular tumor diameters were measured with a caliper on days 1, 3, and 7 after radiation exposure. The tumor volumes were calculated as $V = (\pi/6) \times a$ (mm) × b^2 (mm^2), where a and b are the largest and smallest perpendicular tumor diameters, respectively. Subsequent measurements were normalized to the pretreatment tumor volume.

Statistical analysis

The data are presented as the mean ± SD. All statistical analyses were conducted using Prism 5 (Version 5.0, GraphPad Software, Inc.). Longitudinal relaxation rates ($R_1 = 1/T_1$) before and after $MnCl_2$ administration in the control and radiation-exposed tumors were calculated. We compared control and radiation-exposed groups using the unpaired t test and considered values of $P < 0.05$ to be significant for the *in vitro* Mn-uptake study, tumor size analysis, *in vivo* T_2 quantitative MRI data analysis, and histologic experiments. A one-way ANOVA with Tukey *post hoc* test was applied to compare R_1 values between tumors.

Results

In vitro imaging of tumor cells using MEMRI

Figure 1A shows T_1-weighted MR images of the pellets of colon-26 cells, either exposed or not exposed to radiation, after incubation in a standard medium with or without 0.1 mmol/L $MnCl_2$ supplementation. Irradiated colon-26 cells showed less signal enhancement compared with control colon-26 cells after $MnCl_2$ administration at 24 hours after X-ray irradiation (Fig. 1A). The R_1 values in the irradiated colon-26 cells (0.77 ± 0.01 s^{-1}) were lower than those in the control colon-26 cells (0.82 ± 0.01 s^{-1}) when loaded with 0.1 mmol/L $MnCl_2$ (Fig. 1B; **, $P < 0.01$).

Flow cytometry for the assessment of cell cycle and viability

Figure 2A and B show the results of the flow cytometric cell-cycle analysis. The proportion of G_2–M-phase cells was increased in the radiation-exposed samples (G_2–M of 34.9%; Fig. 2B) in comparison with the control cells (G_2–M of 28.4%; Fig. 2A). Moreover, the proportion of G_0–G_1 phase cells was markedly decreased in the radiation-exposed samples

Published OnlineFirst May 21, 2013; DOI: 10.1158/0008-5472.CAN-12-3837

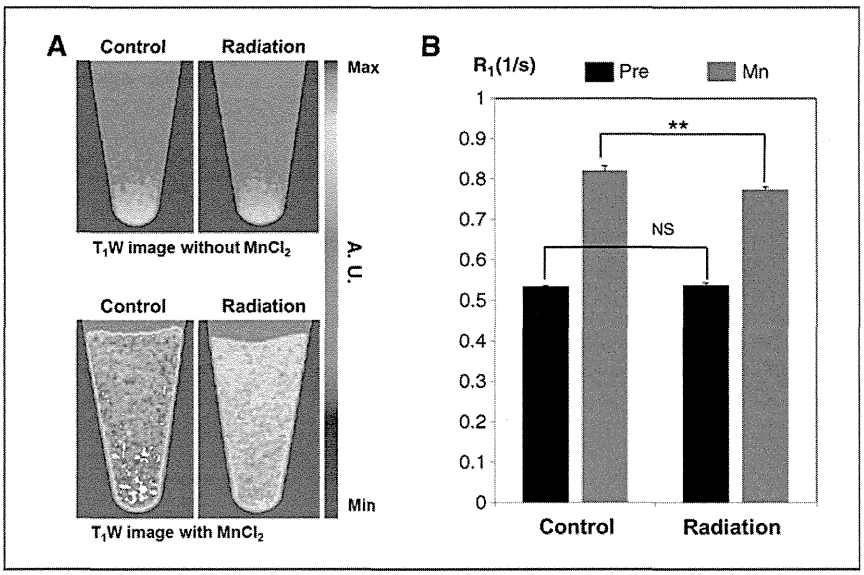

Figure 1. *In vitro* imaging of tumor cells using MEMRI. A, T_1 weighted images of the colon-26 cell pellets with (left) or without (right) X-ray exposure incubated with (top) or without (bottom) 0.1 mmol/L $MnCl_2$. The signal from the control colon-26 cells was enhanced by $MnCl_2$ in comparison with the X-ray–exposed colon-26 cells (top, control). The signal intensity is indicated by the color bar (arbitrary unit). B, R_1 values of the cells. The R_1 values in the X-ray–exposed colon-26 cells were lower than those in the control colon-26 cells when loaded with 0.1 mmol/L $MnCl_2$ (**, $P < 0.01$).

(G_0–G_1 of 1.3%; Fig. 2B) in comparison with the control cells (G_0–G_1 of 22.1%; Fig. 2A). Figure 2C and D show the results of the flow cytometric apoptosis analysis. More apoptotic cells were detected in the radiation-exposed samples (16.8%; Fig. 2D, bottom right, black arrow) in comparison with the control cells (7.1%;Fig. 2C, bottom right).

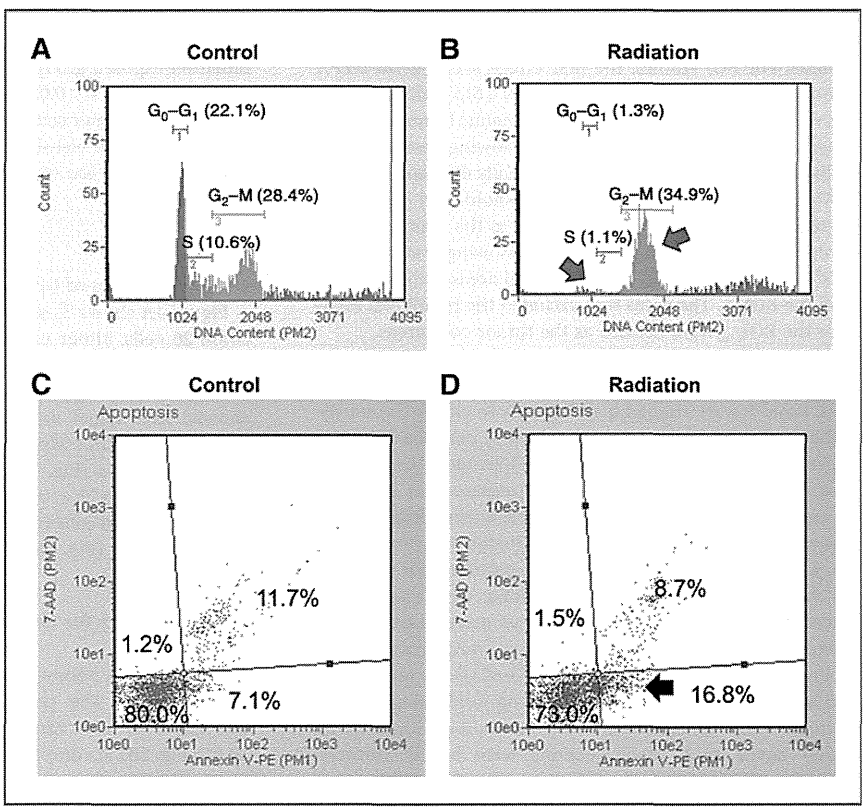

Figure 2. Cell-cycle and cell viability analyses using flow cytometry. A and B, flow cytometric cell-cycle analysis. The proportion of G_2-phase cells was increased in the radiation-exposed samples in comparison with the control samples (red arrow). Moreover, the number of G_0–G_1 phase cells was decreased in the radiation-exposed samples in comparison with the control samples (green arrow). C and D, flow cytometric apoptosis analysis. A greater number of apoptotic cells were detected in the radiation-exposed samples (black arrow) in comparison with the control samples.

Published OnlineFirst May 21, 2013; DOI: 10.1158/0008-5472.CAN-12-3837

Tumor growth

The tumor size ratio with respect to the pretreatment size is shown in Fig. 3 for both groups. There was no significant difference between the tumor sizes of 2 groups 1 day after radiation exposure, although the volume of the irradiated tumor was significantly smaller than that of the control groups on the third and seventh days ($P < 0.001$).

In vivo tumor imaging using MEMRI

We used Gd-DTPA to evaluate tumor vasculature condition and exclude the area where Gd-DTPA was highly accumulated because of disruption of the intratumor microvasculature. The core areas of control and radiation-exposed tumors were homogeneously and almost equally enhanced by Gd-DTPA (Fig. 4A). After disappearance of the Gd-enhancement (typically within 60 minutes), we obtained MEMRI with systemic $MnCl_2$ administration. In contrast to Gd-enhanced MRI, the control tumors were preferentially enhanced by $MnCl_2$ in the

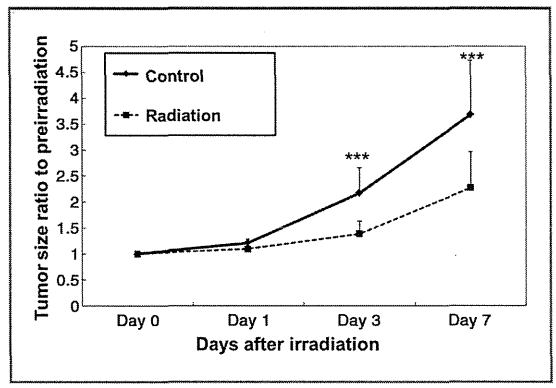

Figure 3. Tumor volume measurements. Tumor growth was significantly retarded in the radiation-exposed group after 3 and 7 days (***, $P < 0.001$). There was no significant difference between the tumor sizes of 2 groups 1 day after treatment.

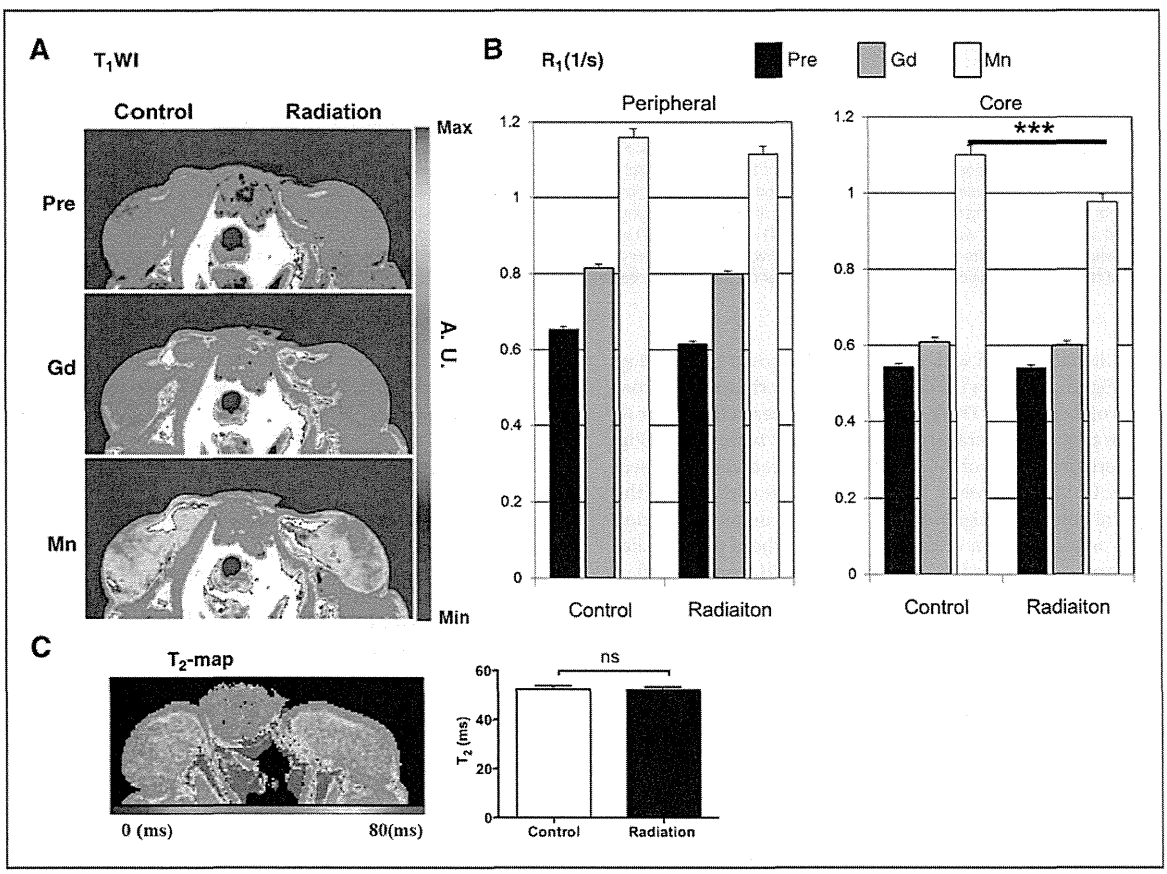

Figure 4. *In vivo* imaging using MEMRI. A, top, control T_1-weighted image. A, middle, Gd-enhanced first T_1-weighted image. A, bottom, Mn-enhanced third T_1-weighted image. The core areas of control and radiation-exposed tumors were homogeneously and almost equally enhanced by Gd-DTPA (A, middle). In MEMRI, the control tumor was preferentially enhanced in comparison with the radiation-exposed tumor following $MnCl_2$ administration (A, bottom). The signal intensity is indicated by the color bar (arbitrary unit). B, the R_1 values in the peripheral area and the core of the tumors. There are no differences in the peripheral area R_1 values between the 2 tumor types. The R_1 values in the core areas of the control tumors were significantly higher at 30 minutes after Mn^{2+} administration than that in the radiation-exposed tumors (***, $P < 0.001$). C, the T_2-map of the X-ray–treated and control tumors. There are no differences between both tumor T_2 values.

Published OnlineFirst May 21, 2013; DOI: 10.1158/0008-5472.CAN-12-3837

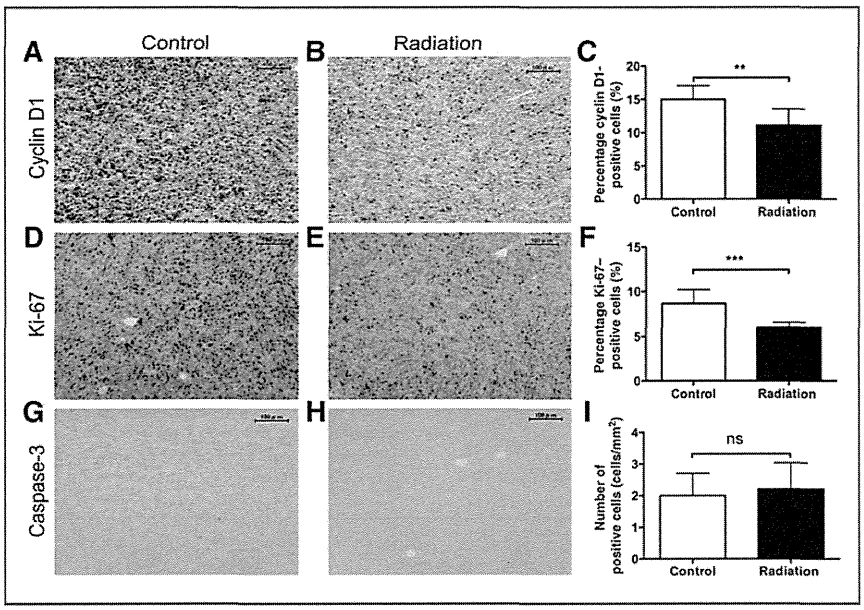

Figure 5. Immunohistochemical staining of tumors. A, cyclin D1 staining of the control tumor core region. B, cyclin D1 staining of the radiation-exposed tumor core region. C, statistical analysis of cyclin D1-positive cells. D, Ki-67 staining of the control tumor core regions. E, Ki-67 staining of the radiation-exposed tumor core regions. F, statistical analysis of Ki-67–positive cells. G, activated caspase-3 staining of the control tumor core regions. H, activated caspase-3 staining of the radiation-exposed tumor core regions. I, statistical analysis of the activated caspase-3–positive cells. These immunohistologic staining results show the detection of cellular alterations in the tumor core at 24 hours following radiation exposure. The number of positively stained cells in the core was decreased for cyclin-D1 (C) and Ki-67 (D vs. E) in exposed colon-26 tumors. The number of Ki-67–positive cells was decreased at 24 hours after radiation exposure (F). However, the number of apoptotic cells was not significantly different between the radiation-exposed and control tumors (I). Magnification, ×200; the black bar on the right represents 100 μm. (**, $P < 0.01$; ***, $P < 0.001$).

T_1WI in comparison with the radiation-exposed tumors (Fig. 4A). Figure 4B shows the R_1 values in the peripheral and core areas of the tumors. There were no differences in the tumor R_1 values in the peripheral areas between the 2 tumor types (Fig. 4B; peripheral: control, $0.61 \pm 0.01\ s^{-1}$ and radiation-exposed, $0.60 \pm 0.01\ s^{-1}$). However, the R_1 values in the core areas of the control tumor were significantly higher at 30 minutes following Mn^{2+} administration in comparison with those of the radiation-exposed tumors (Fig. 4B; core, $P < 0.001$; control, $1.10 \pm 0.02\ s^{-1}$ and radiation-exposed, $0.97 \pm 0.02\ s^{-1}$). T_2 maps of the radiation-exposed and control tumors were calculated (control, 52.3 ± 1.5 ms; radiation-exposed, 52.1 ± 1.2 ms). There were no differences between the T_2 values of the tumors (Fig. 4C).

Immunohistochemical staining of tumors

Figure 5A–I shows the results of the immunohistochemical staining for the evaluation of cellular alterations in the tumor core 24 hours after radiation exposure. The immunohistologic stainings for cyclin D1 and Ki-67 indicated that both cell cycle and proliferation in the radiation-exposed tumor core were significantly changed (Fig. 5C; cyclin D1, $P < 0.01$: control, $14.9 \pm 2.0\%$ and radiation-exposed, $11.0 \pm 2.4\%$, $P < 0.01$; and Fig. 5F; Ki-67: control, $8.6 \pm 1.6\%$ and radiation-exposed, $5.9 \pm 0.6\%$, $P < 0.001$). On the other hand, the number of apoptotic cells per section was not significantly different between the radiation-exposed and control tumors (Fig. 5I, control: 2.0 ± 0.7 and radiation exposed: 2.2 ± 0.8).

Discussion

Relationship between radiation-induced cell-cycle alteration and Mn^{2+} uptake

Ca^{2+} is required to maintain normal structure and function in all living cells (22) and participates in a variety of physiologic and biologic events such as proliferation and apoptosis (23). *In vitro* calcium imaging is a common technique frequently carried out in studies that are designed to show the Ca^{2+} status of a tissue or a medium. In particular, the dynamics of intracellular Ca^{2+} can only be analyzed by optical methods using calcium-sensitive dyes for the detection of Ca^{2+}-bound fluorescence *in vitro* (24). Recently, *in vivo* MEMRI has provided a unique opportunity to study neuronal activation and architecture due to the ability of Mn^{2+} as a calcium surrogate (10–12). Mn^{2+} can enter cells via the same transport systems as those used by Ca^{2+} and can bind to a number of intracellular structures with high-affinity Ca^{2+}- and Mg^{2+}-binding sites on proteins and nucleic acids (25). Mn^{2+} as a positive contrast agent in T_1W MRI has long been used in many biologic applications for brain mapping (26), brain disease (12) (27), neuronal tract tracing (28), and cardiac functional studies (29).

Published OnlineFirst May 21, 2013; DOI: 10.1158/0008-5472.CAN-12-3837

Although several factors influencing Mn^{2+} uptake in cells have been reported such as voltage-gated Ca^{2+}-channel activities (30–33), NMDA (14) and calcium-sensing receptor (34) expression, astroglia (27) and microglia (35) activity/cellularity, activities of enzymes (e.g., manganese superoxide dismutase; refs. 36, 37) and metal transporters, the mechanisms involved in Mn^{2+} uptake in tumor cells are not well known. Some previous studies have shown that MEMRI can enhance some types of tumors *in vivo*, such as salivary gland and eye (choroidal) tumors (16, 17). In particular, Braun and colleagues showed that the uptake of Mn^{2+} by tumors depends on the cell-proliferation rate (18). Thus, we conducted a $MnCl_2$ loading study to investigate whether Mn^{2+} is accumulated in tumor cells that have undergone G_2–M cell-cycle arrest due to radiation exposure. Mn^{2+} accumulation was decreased in radiation-exposed tumor cells both *in vitro* and *in vivo* (Fig. 1B and Fig. 4A) with cell-cycle alteration as early as 24 hours after irradiation, when insignificant increase in apoptotic cells was observed (Fig. 2D and Fig. 5C). These results suggest that the cell-cycle alteration of tumor cells is an important determinant of the uptake of Mn2+ in MEMRI, and that the apoptosis of tumor cells is not a predominant factor in the decrease of Mn2+ uptake for our the 20-Gy radiation condition. At most, less than 10% increment in the number of apoptotic cells may induce a small signal reduction.

Intracellular free Ca^{2+} has been proposed to play a role in the regulation of the cell cycle (38) and in the progression into mitosis from the G_2 arrest point (39). In the late G_2 phase, cells with activated cdc2 kinase can enter into mitosis (40). However, radiation exposure induces a significant G_2 cell-cycle arrest (5, 41) and decreased functioning of cdc2 kinase (41). The local transient increase in free Ca^{2+} influences the rate of cdc2 kinase activation, and it is necessary to initiate pathways leading to cdc2 kinase inactivation in the mitotic cell cycle (42). Therefore, we suggest that the decrease in Ca^{2+} uptake due to inactivated cdc2 kinase contributes to MEMRI signal reduction in the radiation-exposed model.

Factors involved in Mn^{2+} uptake in radiation-exposed tumor cells

Other factors can alter the uptake of the Mn^{2+} contrast agent in tumor cells. For example, cell viability (apoptotic or necrotic change) and density affect Mn^{2+} uptake in MEMRI. Hu and colleagues showed that Mn^{2+} acts as a viability marker depending on Ca^{2+}-channel activity in myocardial ischemia (29). This result suggests that living cells can accumulate higher amount of Mn^{2+} than infracted cells. In our study, neither apoptosis nor necrosis was detected in the *in vivo* radiation-exposed or control tumors (Figs. 4C and 5I). In addition, exclusion of apoptotic cells from radiation-exposed tumor cells using a cell sorter did not strongly affect the MRI signal in comparison with that from non-sorted irradiated cells *in vitro* (Supplementary Fig. S1). In contrast, cell-cycle alterations were clearly detected in both *in vitro* and *in vivo* irradiated tumor cells using flow cytometry (Fig. 2) and cyclin D1 staining (Figs. 2 and 5C). Although apoptosis and apoptotic stimuli are linked to cell-cycle regulators (43), under the condition of our radiation dose and tumor model, apoptosis-altered cells did not significantly affect the MRI signal because the number of apoptotic cells was comparatively small.

In previous work, it was reported that Mn^{2+} uptake in the tumor is linked to the proliferation rate of tumor cells (18). In our study, the number of Ki-67–positive cells (potential marker of tumor growth activity; refs. 44, 45) and the MEMRI signal were decreased at 24 hours after irradiation (Fig. 5F). The Ki-67 (Fig. 5) and MEMRI observations agreed well with a previous report (18) and suggested that the Mn^{2+} accumulation in tumors, when evaluated during the early phase (24 hours) after irradiation, reflects cell-cycle alteration and a subsequent decrease in cell proliferation rather than apoptotic alterations.

Tumor vascularization is an important factor that affects the uptake of contrast agents in tumor-bearing animals. We evaluated vasculature conditions inside the tumor using an extracellular Gd-DTPA contrast agent before all MEMRI experiments (Gd-DTPA does not affect the MEMRI signal because the extracellular agent is not accumulated in the tumor and is rapidly excreted within approximately 1 hour after administration). In most cases, there was no regional enhancement inside tumors, either with or without radiation exposure, after Gd-DTPA administration (Fig. 4A). In addition, dynamic contrast-enhanced MRI (Supplementary Fig. *S2*; tumor microcirculation) and CD-31 immunohistologic staining (Supplementary Fig. *S4*; structure of vascular endothelial cells) showed that there was no significant difference in the vessel structure between the control and radiation-exposed tumors. Therefore, the 20-Gy radiation exposure for the colon-26 tumor cells did not damage the microvessel structure at 1 day *in vivo*. Consequently, it is thought that vasculature disruption in the tumor did not affect the MEMRI signal at 1 day in our model. In addition, necrotic or inflammatory alterations and bleeding in the tumors were not observed based on the T_2 values (Fig. 4C) and hematoxylin and eosin (H&E) staining (Supplementary Fig. *S3*).

In conclusion, we used MEMRI to observe the Mn^{2+} uptake in X-ray–exposed models of *in vitro* tumor cells and an *in vivo* tumor-bearing animal model. The irradiated colon-26 tumor cells underwent cell-cycle alterations (leading to decreased proliferation) but did not exhibit serious apoptotic/necrotic/inflammatory alterations or vascular damage early after irradiation. MEMRI and quantitative maps of the relaxation rate (R_1) map showed a significant signal reduction both *in vitro* and *in vivo*. Our data provides evidence that MEMRI will be a useful tool for the early evaluation and optimization of radiotherapy in the near future, enabling the imaging of cell-cycle arrest and the associated suppression of cell proliferation *in vivo*.

Disclosure of Potential Conflicts of Interest

No potential conflicts of interest were disclosed.

Authors' Contributions

Conception and design: S. Saito, S. Hasegawa, I. Aoki
Development of methodology: S. Saito, I. Aoki
Acquisition of data (provided animals, acquired and managed patients, provided facilities, etc.): S. Saito, S. Hasegawa, A. Sekita
Analysis and interpretation of data (e.g., statistical analysis, biostatistics, computational analysis): S. Saito, S. Hasegawa, A. Sekita, I. Aoki

Published OnlineFirst May 21, 2013; DOI: 10.1158/0008-5472.CAN-12-3837

Writing, review, and/or revision of the manuscript: S. Saito, S. Hasegawa, R. Bakalova, T. Furukawa, T. Saga, I. Aoki
Administrative, technical, or material support (i.e., reporting or organizing data, constructing databases): S. Saito, A. Sekita
Study supervision: S. Saito, R. Bakalova, K. Murase, T. Saga, I. Aoki

Acknowledgments

The authors thank Sayaka Shibata, Takeo Shimomura, and Jeff Kershaw (National Institute of Radiological Sciences, Japan) for technical assistance and discussions. The authors also thank Takeshi Maeda, Hiroyuki Takano, and the FACS support team of the National Institute of Radiological Sciences for their technical assistance during the experiments using flow cytometry.

Grant Support

This work was partly supported by Grants-in-Aid for Scientific Research (Kakenhi) of the Japan Society for the Promotion of Science (JSPS) and the Funding Program for World-Leading Innovative R&D on Science and Technology (FIRST Program).

The costs of publication of this article were defrayed in part by the payment of page charges. This article must therefore be hereby marked *advertisement* in accordance with 18 U.S.C. Section 1734 solely to indicate this fact.

Received October 10, 2012; revised February 19, 2013; accepted March 6, 2013; published OnlineFirst May 21, 2013.

References

1. Greco C, Wolden S. Current status of radiotherapy with proton and light ion beams. Cancer 2007;109:1227–38.
2. Jones B. The potential clinical advantages of charged particle radiotherapy using protons or light ions. Clin Oncol (R Coll Radiol) 2008; 20:555–63.
3. Miyamoto T [Heavy ion therapy for non–small cell lung cancer–new, radical radiotherapy for advanced-age patients as an alternative to surgery]. Gan To Kagaku Ryoho 2003;30:209–14.
4. Kanematsu N, Asakura H, Kohno R, Takahashi O. Tumour shapes and fully automated range compensation for heavy charged particle radiotherapy. Phys Med Biol 2004;49:N1–5.
5. Wilson GD, Martindale CA, Soranson JA, Bourhis J, Carl UM, McNally NJ. Radiation-induced cell cycle delay measured in two mouse tumors *in vivo* using bromodeoxyuridine. Radiat Res 1994; 137:177–85.
6. Di Leonardo A, Linke SP, Clarkin K, Wahl GM. DNA damage triggers a prolonged p53-dependent G1 arrest and long-term induction of Cip1 in normal human fibroblasts. Genes Dev 1994;8:2540–51.
7. Suzuki K, Mori I, Nakayama Y, Miyakoda M, Kodama S, Watanabe M. Radiation-induced senescence-like growth arrest requires TP53 function but not telomere shortening. Radiat Res 2001;155:248–53.
8. DeSimone JN, Dolezalova H, Redpath JL, Stanbridge EJ. Prolonged cell cycle arrest in irradiated human diploid skin fibroblasts: the role of nutrient deprivation. Radiat Res 2000;153:131–43.
9. Dimri GP, Lee X, Basile G, Acosta M, Scott G, Roskelley C, et al. A biomarker that identifies senescent human cells in culture and in aging skin *in vivo*. Proc Natl Acad Sci U S A 1995;92:9363–7.
10. Koretsky AP, Silva AC. Manganese-enhanced magnetic resonance imaging (MEMRI). NMR Biomed 2004;17:527–31.
11. Silva AC, Lee JH, Aoki I, Koretsky AP. Manganese-enhanced magnetic resonance imaging (MEMRI): methodological and practical considerations. NMR Biomed 2004;17:532–43.
12. Aoki I, Naruse S, Tanaka C. Manganese-enhanced magnetic resonance imaging (MEMRI) of brain activity and applications to early detection of brain ischemia. NMR Biomed 2004;17:569–80.
13. Aschner M. Manganese homeostasis in the CNS. Environ Res 1999;80:105–9.
14. Itoh K, Sakata M, Watanabe M, Aikawa Y, Fujii H. The entry of manganese ions into the brain is accelerated by the activation of *N*-methyl-D-aspartate receptors. Neuroscience 2008;154:732–40.
15. Pautler RG, Koretsky AP. Tracing odor-induced activation in the olfactory bulbs of mice using manganese-enhanced magnetic resonance imaging. Neuroimage 2002;16:441–8.
16. Seshadri M, Hoy A. Manganese-enhanced MRI of salivary glands and head and neck tumors in living subjects. Magn Reson Med 2010; 64:902–6.
17. Braun RD, Gradianu M, Vistisen KS, Roberts RL, Berkowitz BA. Manganese-enhanced MRI of human choroidal melanoma xenografts. Invest Ophthalmol Vis Sci 2007;48:963–7.
18. Braun RD, Bissig D, North R, Vistisen KS, Berkowitz BA. Human tumor cell proliferation evaluated using manganese-enhanced MRI. PLoS ONE 2012;7:e30572.
19. Hu TC, Bao W, Lenhard SC, Schaeffer TR, Yue TL, Willette RN, et al. Simultaneous assessment of left-ventricular infarction size, function and tissue viability in a murine model of myocardial infarction by cardiac manganese-enhanced magnetic resonance imaging (MEMRI). NMR Biomed 2004;17:620–6.
20. Waghorn B, Schumacher A, Liu J, Jacobs S, Baba A, Matsuda T, et al. Indirectly probing Ca(2+) handling alterations following myocardial infarction in a murine model using T(1)-mapping manganese-enhanced magnetic resonance imaging. Magn Reson Med 2011;65: 239–49.
21. Inanami O, Iizuka D, Iwahara A, Yamamori T, Kon Y, Asanuma T, et al. A novel anticancer ribonucleoside, 1-(3-C-ethynyl-beta-D-ribo-pentofuranosyl)cytosine, enhances radiation-induced cell death in tumor cells. Radiat Res 2004;162:635–45.
22. Barrett PQ, Kojima I, Kojima K, Zawalich K, Isales CM, Rasmussen H. Short term memory in the calcium messenger system. Evidence for a sustained activation of protein kinase C in adrenal glomerulosa cells. Biochem J 1986;238:905–12.
23. Capiod T, Shuba Y, Skryma R, Prevarskaya N. Calcium signalling and cancer cell growth. Subcell Biochem 2007;45:405–27.
24. Dawitz J, Kroon T, Hjorth JJ, Meredith RM. Functional calcium imaging in developing cortical networks. J Vis Exp 2011;56:e3550.
25. Mihai R, Stevens J, McKinney C, Ibrahim NB. Expression of the calcium receptor in human breast cancer–a potential new marker predicting the risk of bone metastases. Eur J Surg Oncol 2006;32:511–5.
26. de Sousa PL, de Souza SL, Silva AC, de Souza RE, de Castro RM. Manganese-enhanced magnetic resonance imaging (MEMRI) of rat brain after systemic administration of $MnCl_2$: changes in T1 relaxation times during postnatal development. J Magn Reson Imaging 2007; 25:32–8.
27. Kawai Y, Aoki I, Umeda M, Higuchi T, Kershaw J, Higuchi M, et al. *In vivo* visualization of reactive gliosis using manganese-enhanced magnetic resonance imaging. Neuroimage 2010;49:3122–31.
28. Pautler RG. *In vivo*, trans-synaptic tract-tracing utilizing manganese-enhanced magnetic resonance imaging (MEMRI). NMR Biomed 2004; 17:595–601.
29. Hu TC, Christian TF, Aletras AH, Taylor JL, Koretsky AP, Arai AE. Manganese enhanced magnetic resonance imaging of normal and ischemic canine heart. Magn Reson Med 2005;54:196–200.
30. Anderson M. Mn ions pass through calcium channels. A possible explanation. J Gen Physiol 1983;81:805–27.
31. Narita K, Kawasaki F, Kita H. Mn and Mg influxes through Ca channels of motor nerve terminals are prevented by verapamil in frogs. Brain Res 1990;510:289–95.
32. Lin YJ, Koretsky AP. Manganese ion enhances T1-weighted MRI during brain activation: an approach to direct imaging of brain function. Magn Reson Med 1997;38:378–88.
33. Kita H, Narita K, Van der Kloot W. Tetanic stimulation increases the frequency of miniature end-plate potentials at the frog neuromuscular junction in Mn^{2+}-, CO^{2+}-, and Ni^{2+}-saline solutions. Brain Res 1981;205:111–21.
34. Baio G, Fabbi M, Emionite L, Cilli M, Salvi S, Ghedin P, et al. *In vivo* imaging of human breast cancer mouse model with high level expression of calcium sensing receptor at 3T. Eur Radiol 2012;22:551–8.
35. Wideroe M, Olsen O, Pedersen TB, Goa PE, Kavelaars A, Heijnen C, et al. Manganese-enhanced magnetic resonance imaging of hypoxic–ischemic brain injury in the neonatal rat. Neuroimage 2009; 45:880–90.

Published OnlineFirst May 21, 2013; DOI: 10.1158/0008-5472.CAN-12-3837

36. Hasegawa S, Koshikawa-Yano M, Saito S, Morokoshi Y, Furukawa T, Aoki I, et al. Molecular imaging of mesothelioma by detection of manganese-superoxide dismutase activity using manganese-enhanced magnetic resonance imaging. Int J Cancer 2011;128:2138–46.
37. Hasegawa S, Saito S, Koshikawa-Yano M, Furukawa T, Aoki I, Saga T. Tumor enhancement effect of overexpressed manganese-superoxide dismutase in manganese-enhanced MR imaging. Magn Reson Med Sci 2011;10:155–8.
38. Wahl M, Gruenstein E. Intracellular free Ca2+ in the cell cycle in human fibroblasts: transitions between G1 and G0 and progression into S phase. Mol Biol Cell 1993;4:293–302.
39. Lu KP, Osmani SA, Osmani AH, Means AR. Essential roles for calcium and calmodulin in G2/M progression in *Aspergillus nidulans*. J Cell Biol 1993;121:621–30.
40. Kishimoto T, Okumura E. *In vivo* regulation of the entry into M-phase: initial activation and nuclear translocation of cyclin B/Cdc2. Prog Cell Cycle Res 1997;3:241–9.
41. Crompton NE, Hain J, Jaussi R, Burkart W. Staurosporine- and radiation-induced G2-phase cell cycle blocks are equally released by caffeine. Radiat Res 1993;135:372–9.
42. Lindsay HD, Whitaker MJ, Ford CC. Calcium requirements during mitotic cdc2 kinase activation and cyclin degradation in *Xenopus* egg extracts. J Cell Sci 1995;108 (Pt 11):3557–68.
43. Alenzi FQ. Links between apoptosis, proliferation and the cell cycle. Br J Biomed Scie 2004;61:99–102.
44. Cuzick J, Dowsett M, Pineda S, Wale C, Salter J, Quinn E, et al. Prognostic value of a combined estrogen receptor, progesterone receptor, Ki-67, and human epidermal growth factor receptor 2 immunohistochemical score and comparison with the genomic health recurrence score in early breast cancer. J Clin Oncol 2011; 29:4273–8.
45. Liu J, Li Z, Cui J, Xu G, Cui G. Cellular changes in the tumor microenvironment of human esophageal squamous cell carcinomas. Tumour Biol 2011;33:495–505.

Journal of Controlled Release 169 (2013) 220–227

Contents lists available at SciVerse ScienceDirect

Journal of Controlled Release

journal homepage: www.elsevier.com/locate/jconrel

SPIO-PICsome: Development of a highly sensitive and stealth-capable MRI nano-agent for tumor detection using SPIO-loaded unilamellar polyion complex vesicles (PICsomes)

Daisuke Kokuryo [a,1], Yasutaka Anraku [b,1], Akihiro Kishimura [b,*], Sayaka Tanaka [c], Mitsunobu R. Kano [c], Jeff Kershaw [a], Nobuhiro Nishiyama [d], Tsuneo Saga [a], Ichio Aoki [a,**], Kazunori Kataoka [b,e,***]

[a] Molecular Imaging Center, National Institute of Radiological Sciences, Chiba-city 263-8555, Japan
[b] Department of Materials Engineering, Graduate School of Engineering, The University of Tokyo, Tokyo 113-8656, Japan
[c] Department of Pharmaceutical Biomedicine, Graduate School of Medicine, Dentistry and Pharmaceutical Sciences, Okayama University, Okayama 700-8530, Japan
[d] Polymer Chemistry Division, Chemical Resources Laboratory, Tokyo Institute of Technology, Yokohama 226-8503, Japan
[e] Center for Disease Biology and Integrative Medicine, Graduate School of Medicine, The University of Tokyo, Tokyo 113-8656, Japan

ARTICLE INFO

Article history:
Received 1 December 2012
Accepted 22 March 2013
Available online 29 March 2013

Keywords:
Polyion complex vesicles (PICsomes)
Magnetic resonance imaging (MRI)
Superparamagnetic iron oxide nanoparticles (SPIOs)
Drug delivery system
Tumor diagnosis

ABSTRACT

Size controllable polyion complex vesicles (PICsomes), composed of biocompatible poly(ethylene glycol) (PEG) and poly(amino acid)s, have an extremely prolonged lifetime in the bloodstream that enables them to accumulate effectively in tumors via the enhanced permeability and retention (EPR) effect. The purpose of this study was to use PICsomes to synthesize a highly sensitive MRI contrast agent for more precise tumor detection. We synthesized SPIO-Cy5-PICsomes (superparamagnetic iron oxide nanoparticle-loaded Cy5-cross-linked Nano-PICsomes) and characterized them using dynamic light scattering and transmission electron microscopy *in vitro* and evaluated their ability to detect subcutaneously grafted tumors *in vivo* with MRI. The transverse relaxivity (r_2) of the SPIO-Cy5-PICsomes ($r_2 = 663 \pm 28$ mM^{-1} s^{-1}) was 2.54 times higher than that of bare clinically-used SPIO. In *in vivo* MRI experiments on mice subcutaneously grafted with colon-26 tumor cells, the tumor signal was significantly altered at 3 h after SPIO-Cy5-PICsome administration and persisted for at least 24 h. Small and early-stage *in vivo* tumors (3 days after grafting, approximately 4 mm^3) were also clearly detected with MRI. SPIO-loaded PICsomes are sensitive MRI contrast agents that can act as a powerful nanocarrier to detect small tumors for early diagnosis.

1. Introduction

The detection of early-stage tumors, especially during the early phase of metastasis, is important for improving treatment efficacy and prolonging patient survival. Non-invasive *in vivo* imaging, such as with magnetic resonance imaging (MRI) and positron emission tomography (PET), is critical for detecting disease in its early phase, and for that reason many biomedical applications utilize these techniques [1]. One advantage that MRI has over PET is that it can image at higher spatial resolutions [2]. However, low sensitivity to exogenous molecular probes (contrast agents) is a major limitation of MRI in comparison with PET. It is therefore necessary to engineer the properties of the probe to optimize its sensitivity for MRI.

Carboxyl dextran-coated superparamagnetic iron oxide (SPIO) nanoparticles are good 'negative' contrast agents for improving MRI contrast and have been used for clinical diagnosis and in pre-clinical cancer studies [3,4]. In clinical research, commercial SPIO nanoparticles, such as ferucarbotran (Resovist®) or ferumoxides (Feridex®), have been applied to detect metastatic tumors in the liver [5–8]. Unfortunately, carboxyl dextran-coated SPIO by itself does not have the ability to target tumors because Kupffer cells in healthy regions of the liver capture the SPIOs, with the result that the majority of the effect on the MRI signal occurs in the liver rather than in the tumor regions [6,7]. Therefore, to target tumors directly with SPIO nanoparticles, it is necessary to add a 'stealth' property in order to avoid recognition by the reticuloendothelial system (RES) and increase the lifetime of SPIOs in the bloodstream [3,9].

One strategy to achieve this stealth capability is to encapsulate the SPIOs in other nanoparticles that have prolonged lifetimes in the bloodstream and can passively accumulate in tumors due to the enhanced permeability and retention (EPR) effect [10]. Biocompatible poly(ethylene glycol) (PEG)-conjugated SPIOs or SPIO-loaded

* Correspondence to: A. Kishimura, 7-3-1 Hongo, Bunkyo-ku, Tokyo 113-8656, Japan. Tel.: +81 3 5841 7109; fax: +81 3 5841 7139.
** Correspondence to: I. Aoki, 4-9-1 Anagawa, Inage-ku, Chiba-city 263-8555, Japan. Tel.: +81 43 206 3272; fax: +81 43 206 3276.
*** Correspondence to: K. Kataoka, 7-3-1 Hongo, Bunkyo-ku, Tokyo 113-8656, Japan. Tel.: +81 3 5841 7138; fax: +81 3 5841 7139.
E-mail addresses: kishimura@bmw.t.u-tokyo.ac.jp (A. Kishimura), aoki@nirs.go.jp (I. Aoki), kataoka@bmw.t.u-tokyo.ac.jp (K. Kataoka).
[1] These two authors contributed equally.

0168-3659/$ – see front matter © 2013 Elsevier B.V. All rights reserved.
http://dx.doi.org/10.1016/j.jconrel.2013.03.016

nano-carriers have previously been employed to target tumors with SPIOs, with the targeting strategies falling into the following three groups: 1) PEG-conjugated SPIOs [11–15], 2) Ultra-small SPIO (USPIO)-loaded PEGylated micelles [16–20], and 3) SPIO-loaded PEGylated nano-vesicles [21–23]. Although the use of PEG-conjugated SPIOs is a simple strategy to prevent rapid clearance from the bloodstream, the direct conjugation of PEG to clinically-used SPIOs still has several drawbacks. First, stable and highly dense conjugation of PEG chains on the surface of SPIOs is technically difficult because the conjugation between PEG chains and carboxyl dextran is not stable, especially in the bloodstream. Accordingly, some additional surface modifications are required to achieve stable conjugation between PEG and SPIO nanoparticles [24]. Another drawback is that PEG-conjugated SPIOs have limited internal space, making it difficult to load them with drug levels sufficient for future therapeutic applications.

USPIO-loaded polymeric micelles have a moderately long blood half-life, and the high density of USPIOs that can be loaded into the micelle core noticeably alters the signal in comparison to dispersed USPIOs. It is unfortunate that when loaded with larger diameter SPIOs the micelles have an inadequate lifetime in the physiological environment of the bloodstream. On the other hand, SPIO-loaded PEGylated nano-vesicles, such as stealth liposomes, are designed to have longer circulation in the bloodstream and can be loaded with multiple iron-oxide particles, even if the particles are coated with carboxyl dextran [21–23]. In general, iron-oxide particles of larger size (SPIO > USPIO) or at a higher concentration can induce a greater signal change in T_2-weighted MRI due to T_2 and T_2^* shortening [25,26]. Thus, SPIO-loaded nano-vesicles may significantly enhance the contrast while simultaneously maintaining a high level of clinical safety and an increased blood half-life [27–30].

Recognizing the advantages of PEGylated nano-vesicles, we have developed and optimized polyion complex (PIC) nano-vesicles, called PICsomes. The PICsomes are generated by mixing water-soluble and oppositely charged block copolymers composed of biocompatible PEG and poly(amino acid)s in an aqueous medium [31–34]. PICsomes are characterized by the facile encapsulation of bio-macromolecules, such as dextran and proteins, and long-term retention and protection of cargo, regardless of external influences [32]. More recently, we have succeeded in preparing nano-sized PICsomes (Nano-PICsomes) with a unilamellar PIC membrane [33]. Unlike liposomal nano-carriers, the size of the Nano-PICsomes can be controlled with precision between 100 and 400 nm. After cross-linking the PIC layer via amide coupling of ion pairs, Nano-PICsomes remain in the blood circulation of mice for an extremely long time [34]. The blood lifetime of cross-linked Nano-PICsomes is comparable to that of typical long-lived liposomes and polymersomes [35]. Cross-linked Nano-PICsomes with diameters of approximately 100 nm also show excellent tumor accumulation due to the EPR effect [10]. However, the *in vivo* behavior of Nano-PICsomes containing payloads of contrast agents has not yet been evaluated.

Here, we report the first example of an MRI contrast agent using Nano-PICsomes, named 'SPIO-loaded Cy5-cross-linked Nano-PICsomes (SPIO-Cy5-PICsomes)', which enables targeted tumor imaging. SPIO-Cy5-PICsomes, which we designed and synthesized, are created from the combination of Nano-PICsomes and FDA-approved SPIO nanoparticles. The *in vitro* and *in vivo* performance of SPIO-Cy5-PICsomes was evaluated and characterized for a colon tumor, which is the third most common cancer in both men and women, in a subcutaneous transplanted mouse model. We also investigated the detection of small and early-phase tumors in a similar mouse model.

2. Materials and methods

2.1. Materials

1-ethyl-3-(3-dimethylaminopropyl) carbodiimide hydrochloride (EDC) was purchased from Wako Pure Chemical Industries (Osaka, Japan). A Cy5 mono-reactive dye pack and Sephacryl™ S-1000 gel were purchased from GE Healthcare (Tokyo, Japan). Block-aniomer, PEG-*b*-poly(α,β-aspartic acid) (PEG-PAsp, *Mn* of PEG = 2000, degree of polymerization (DP) of PAsp = 75) and homo-catiomer, poly([5-aminopentyl]-α,β-aspartamide) (Homo-P(Asp-AP), DP of P(Asp-AP) = 82) and Cy5-labeled PEG-PAsp (Cy5-PEG-PAsp) were prepared as previously reported [33]. Ferucarbotran (Resovist®) was purchased from Fujifilm RI Pharma (Tokyo, Japan).

2.2. Preparation and characterization of SPIO-Cy5-PICsomes

Solutions of Cy5-PEG-PAsp (2 mg/mL) and Homo-P(Asp-AP) (1 mg/mL) were prepared separately in 10 mM phosphate buffer (PB, pH 7.4, 0 mM NaCl). A ferucarbotran solution (Fe concentration = 2.9 mg/mL) was mixed with an equal volume of the Cy5-PEG-PAsp to prepare a Cy5-PEG-PAsp/SPIO solution (final concentrations: Cy5-PEG-PAsp, 1 mg/mL; and ferucarbotran, 1.5 mg/mL). Subsequently, the Cy5-PEG-PAsp/SPIO solution was mixed with the Homo-P(Asp-AP) solution with an equal unit ratio of $-COO^-$ and $-NH_3^+$ in the charged polymers and then vigorously stirred with a vortex mixer to prepare SPIO-Cy5-PICsomes. The SPIO-Cy5-PICsome solution was then added to the EDC solution (10 mg/mL, 10 eqv. per –COOH group in Cy5-PEG-PAsp). After 12 h, the mixed solution was purified using preparative gel permeation chromatography (GPC, column: Sephacryl™ S-1000, GE Healthcare UK, England). The size of the PICsomes was evaluated by dynamic light scattering (DLS) measurements at 25 °C using a Zetasizer Nano-ZS instrument (Malvern Instruments, Malvern, UK) equipped with a He-Ne ion laser (λ = 633 nm). The Fe content of the SPIO-Cy5-PICsomes was 16.1 ± 0.5 mM, as determined by inductively coupled plasma-mass spectroscopy (ICP-MS) performed with a 4500 ICP-MS instrument (Hewlett Packard, Palo Alto, CA, USA).

2.3. Transmission electron microscopy (TEM)

TEM was performed on a HITACHI H-7000 electron microscope operating at 75 kV. Copper grids of 400-mesh were coated with a thin film of formvar, followed by subsequent coating with carbon. Then, 1 μL of the sample solution was placed on the resulting grids and dried at room temperature. The samples were stained by the deposition of a drop of a 50% ethanol solution containing 2 wt.% uranyl acetate onto the surface of the sample-loaded grid and dried at room temperature.

2.4. R_2 and r_2 measurement in vitro

To measure the transverse relaxation rate (R_2), which is the reciprocal of the transverse relaxation time (T_2), of water protons (^1H) in the presence or absence of SPIO-Cy5-PICsomes, an *in vitro* MRI measurement was performed for SPIO-Cy5-PICsomes and bare ferucarbotran (n = 3). The SPIO-Cy5-PICsomes, diluted with phosphate-buffered saline, were prepared and loaded with the same Fe concentrations as control samples of SPIO nanoparticles, and then aliquoted into 0.2 mL PCR tubes. ICP-MS measurements were made to ensure that the Fe concentrations of the SPIO-Cy5-PICsomes and control samples were equal. MRI acquisitions were performed on a 7.0 Tesla, 40 cm bore magnet (Kobelco and Jastec, Kobe, Japan) interfaced to an Avance I system (Bruker-Biospin, Ettlingen, Germany) with a 35-mm diameter volume coil (Rapid Biomedical, Lymper, Germany). The sample temperature was maintained at 23 °C using a gradient-coil cooling system and air conditioners. Two-dimensional multi-spin-echo images were acquired with the following parameters: repetition time (TR)/echo time (TE) = 3000/10–100 ms in steps of 10 ms (10 echoes); field of view (FOV) = 48.0 × 48.0 mm^2; matrix = 256 × 256; resolution = 188 μm × 188 μm; number of slices = 1; slice thickness = 2.0 mm; slice direction = horizontal; and number of acquisitions (NEX) = 1. The scanning time was 12 min 48 s. After image

acquisition, the T_2 and R_2 were estimated using the MRVision image processing software (version 1.6.8, MR vision Co., MA, USA). The transverse relaxivity (r_2) was calculated with the equation; $r_2 = (R_{2obs} - R_{2d})/[Fe]$ (R_{2obs}: R_2 of the sample, R_{2d}: R_2 of the aqueous solution, [Fe]: Fe concentration measured by ICP-MS). Delta R_2 (ΔR_2) maps were calculated as ΔR_2 = (R_2 of the tumor after SPIO-Cy5-PICsome administration) − (R_2 of the tumor before administration).

2.5. Animal and cell line preparation

Overall, nineteen female BALB/c nude mice (Japan SLC, Shizuoka, Japan) were used for all *in vivo* studies. Ten animals were used to evaluate the accumulation of SPIO-Cy5-PICsomes in tumor: five were administered SPIO-Cy5-PICsomes and five were used for the ferucarbotran control. Another three animals were used for small tumor detection. The remaining six animals were used to test the toxicity of the SPIO-Cy5-PICsomes: three were administered SPIO-Cy5-PICsomes and three were used for the ferucarbotran control. The mice were maintained in accordance with the guidelines of the National Institute of Radiological Sciences (NIRS), and all experiments were reviewed and approved by the institute's committee for care and use of laboratory animals.

Colon -26 murine cancer cells were obtained from the RIKEN BioResource Center (Tukuba, Japan). The cells were maintained in Dulbecco's modified Eagle's medium (D5796, Sigma-Aldrich, St Louis, Mo, USA) supplemented with 10% fetal bovine serum, and incubated in a humidified atmosphere of 5% CO_2 in air at 37 °C. After suspension in phosphate-buffered saline, the cells were subcutaneously grafted (1.0×10^6 cells/50 μl) into the left flank of the mice. To measure the initial tumor volume before SPIO-Cy5-PICsome administration, T_2-weighted fast spin-echo images were acquired using a rapid acquisition with relaxation enhancement (RARE) sequence. The imaging parameters were as follows: TR/TE = 2000/40 ms; FOV = 38.4 × 38.4 mm^2; matrix = 256 × 256; resolution = 150 μm × 150 μm; number of slices = 36; slice thickness = 1.0 mm; slice direction = transaxial; RARE factor = 8; and NEX = 2.

2.6. Toxicity test

To evaluate the toxicity of the SPIO-Cy5-PICsomes to mice, the body weight of six BALB/c nude mice (age over 6 weeks-old) was periodically monitored before and after the administration of SPIO-Cy5-PICsomes (n = 3, initial body weight = 17.4 ± 1.2 g) or ferucarbotran (n = 3, initial body weight = 17.9 ± 1.4 g). The SPIO-Cy5-PICsomes or ferucarbotran contained 0.45 mg/kg Fe, which is the dose of ferucarbotran used in the clinic.

2.7. Evaluation of SPIO-Cy5-PICsome accumulation in tumor

To evaluate the *in vivo* tumor accumulation of SPIO-Cy5-PICsomes, 2D multi spin-echo T_2-weighted images were acquired before and after the administration of the SPIO-Cy5-PICsomes. T_2 and R_2 maps were calculated with non-linear least squares fitting to the multi-echo images. The tumors were allowed to grow for 7 to 9 days after the tumor cell transplantation. SPIO-Cy5-PICsomes were intravenously administered to five mice (body weight = 17.9 ± 1.0 g, tumor volume = 107 ± 26 mm^3) in the MRI scanner. The SPIO-Cy5-PICsomes contained 0.45 mg/kg Fe, which is the same as a clinical dose of ferucarbotran. For long-term observation of SPIO-Cy5-PICsome dynamics in tumors, R_2 maps were calculated from multi-spin-echo T_2-weighted images acquired prior to and at 1, 3, 6 and 24 h after administration. After MRI acquisition, *in vivo* fluorescence images were taken using a Maestro EX 2D fluorescence imaging system (PerkinElmer, MA, USA) to confirm the accumulation of SPIO-Cy5-PICsomes in the tumors. The mice were awakened and returned to their cages after all imaging was completed. As a control study, ferucarbotran (Resovist®, 0.45 mg/kg Fe) was injected via the tail vein to a further five mice (body weight = 19.0 ± 1.8 g, tumor volume = 92 ± 40 mm^3).

During the *in vivo* MRI experiments, the rectal temperatures of the mice were monitored using an optical fiber thermometer (FOT-M, FISO Technology, Quebec, Canada) and maintained at approximately 36.5 ± 0.5 °C by warm air provided by a homemade automatic heating system based on an electric temperature controller (E5CN, Omron, Kyoto, Japan). The mice were anesthetized with 1.5–2.0% isoflurane (Escain, Mylan, Tokyo, Japan) gas and a 1:2 O_2:room-air mixture. T_2-weighted images were acquired using a multi-spin-echo sequence with parameters as follows: TR/TE = 3000/10–100 ms in steps of 10 ms (10 echoes); FOV = 38.4 × 19.2 mm^2; matrix = 256 × 128; resolution = 150 μm × 150 μm; number of slices = 9; slice thickness = 1.0 mm; slice gap = 0.5 mm; slice direction = transaxial; and NEX = 1. The scanning time was 6 min 24 s. After image acquisition, the T_2 maps were estimated using MRVision.

In vivo fluorescence images of the mice that received the SPIO-Cy5-PICsomes were acquired using a fluorescent imager (Maestro EX) with the following parameters: excitation filter = 576–621 nm; emission filter = 635 nm longpass; acquisition setting = 630–800 nm in 10 nm steps; acquisition time = 100 ms; and FOV = 12.0 × 12.0 cm^2. After acquisition, unmixed fluorescence information was extracted from the fluorescence spectrum using the Maestro software package (PerkinElmer).

After all imaging was completed for an animal, the grafted tumors were excised and immersed in formalin for histological analysis. The formalin-fixed samples were then paraffinized and thin-sectioned for either hematoxylin and eosin (HE) staining and observation with light microscopy (Keyence, Osaka, Japan), or the Cy5 dye in the accumulated PICsomes was directly observed with a confocal laser scanning microscope (LSM510 META, Carl Zeiss, Oberkochen, Germany).

2.8. Small and early-stage tumor detection

To investigate the possibility of detecting small and early-stage tumors with SPIO-Cy5-PICsomes, we performed *in vivo* MR imaging of three mice 3 days after tumor transplantation. MRI was performed prior to and 24 h after SPIO-Cy5-PICsome administration. The tumor volumes were approximately 4 mm^3 when measured before SPIO-Cy5-PICsome administration.

The MR images were acquired using a 7.0 Tesla, 20 cm bore magnet (Bioscan, Bruker-Biospin) interfaced to an Avance III system with a 2-ch high-sensitivity RF coil (CryoProbe™, Bruker-Biospin). The T_2-weighted images were acquired using a spin-echo sequence with the following parameters: TR/TE = 3000/30 ms; FOV = 25.6 × 12.8 or 19.2 mm^2; matrix = 256 × 128 or 192; resolution = 100 μm × 100 μm; number of slices = 9; slice thickness = 750 μm; slice gap = 250 μm; slice direction = transaxial; and NEX = 2. After MRI acquisition, fluorescence images were also acquired using the same parameters as described in the previous sections.

2.9. Statistical analysis

Alterations to R_2 for the SPIO-Cy5-PICsomes and bare SPIOs were statistically evaluated using a two-way ANOVA with the Bonferroni correction (Prism, Ver. 5, GraphPad Software, CA, USA). Changes to the body weight due to SPIO-Cy5-PICsomes and bare SPIOs were also statistically evaluated with the same test. A significance level of 0.05 was used.

3. Results and discussion

3.1. Chemical characterization of the SPIO-Cy5-PICsomes

The method used to prepare the PICsome nano-carrier was similar to that previously reported for macromolecule-loaded Nano-PICsomes